Lower crustal control in the iron isotope systematics of plutonic xenoliths from Adak Island, Central Aleutians, with implications for arc magma geochemistry

Emma S. Sosa [a,*], Claire E. Bucholz [a], Juan David Hernández-Montenegro [a], Michael A. Kipp [b,1], François L.H. Tissot [b], Barbara C. Ratschbacher [c], Jennifer M. Jackson [a], Suzanne Mahlburg Kay [d], Robert W. Kay [d]

[a] Division of Geological and Planetary Sciences, California Institute of Technology, Pasadena, CA 91125, United States
[b] The Isotoparium, Division of Geological and Planetary Sciences, California Institute of Technology, Pasadena, CA 91125, United States
[c] Department of Earth and Planetary Sciences, University of California, Davis, One Shields Avenue, Davis, CA 95616, United States
[d] Department of Earth and Atmospheric Sciences, Cornell University, Ithaca, NY 14850, United States

ARTICLE INFO

ABSTRACT

We present bulk-rock and mineral Fe isotope data of ultramafic to mafic xenoliths and basaltic to andesitic lavas from Adagdak Volcano (Adak Island, Central Aleutians) to study the effects of early differentiation on the Fe isotopic evolution of island arc basalts and their crystallization products. The Fe isotope composition of ultramafic cumulate xenoliths increases from dunite ($\delta^{56}Fe$ = –0.09 to –0.02 ‰) to clinopyroxenite ($\delta^{56}Fe$ = +0.06 to +0.09 ‰), consistent with higher modal proportions of clinopyroxene ($\delta^{56}Fe$ = –0.05 to +0.11 ‰) relative to olivine ($\delta^{56}Fe$ = –0.10 to +0.06 ‰) in the latter. Mid-crustal cumulate amphibole gabbro and hornblendite cumulates also record heavier Fe isotope compositions ($\delta^{56}Fe$ = +0.04 to +0.08 ‰) due to the abundance of isotopically heavy amphibole ($\delta^{56}Fe$ = +0.07 to +0.09 ‰) and magnetite ($\delta^{56}Fe$ = +0.11 to +0.13 ‰) in these rocks. High inter-mineral fractionations observed in spinel-olivine and spinel-clinopyroxene pairs ($\Delta^{56}Fe_{spl-ol}$ = +0.12 to +0.28 and $\Delta^{56}Fe_{spl-cpx}$ = +0.06 to +0.19) suggest that spinel is not recording equilibrium crystallization conditions for the ultramafic assemblages, likely due to subsolidus Fe-Mg exchange. Our data also include Fe isotope measurements of one mantle dunite ($\delta^{56}Fe$ = +0.03 ± 0.05 ‰). Five Adagdak lavas, spanning from basalts to andesites, yield a narrow range of $\delta^{56}Fe$ between +0.03 and +0.06 ‰. Our results highlight the potential of amphibole in driving the Fe isotope depletion trends observed in many erupted arc lavas, as amphibole hosts 28–99 % of the FeO_T budget in the amphibole gabbro and hornblendite cumulates. This is also supported by single-crystal synchrotron Mössbauer spectroscopy of two amphibole grains, the first from an amphibole gabbro and the second from a hornblendite, which yield $Fe^{3+}/\Sigma Fe$ ratios of 0.55 ± 0.06 and 0.58 ± 0.02, respectively. Water content and hydrogen isotope compositions determined by secondary-ion mass spectrometry from the same amphibole grains indicate partial dehydrogenation. Using Rayleigh fractionation modeling to account for oxidation during post-crystallization dehydrogenation, we calculate magmatic $Fe^{3+}/\Sigma Fe$ ratios of 0.41 ± 0.04 for the amphibole gabbro and 0.30 ± 0.05 for the hornblendite. These data are then used to estimate an appropriate Fe force constant for Adagdak amphibole and quantitatively evaluate the effects of amphibole fractionation. Through a fractional crystallization model, we show how arc melts may experience periods of increasing $\delta^{56}Fe$ during olivine-dominated fractionation, followed by decreasing $\delta^{56}Fe$ once magnetite and amphibole saturate as cumulate phases. Notably, this dichotomy between fractionation of isotopically light versus heavy cumulate assemblages and its effects on the Fe isotope evolution of arc magmas is not captured by the Adagdak lava record, highlighting the utility of cumulates in chronicling the early isotopic evolution of magmatic systems.

* Corresponding author.
  E-mail address: esosa@caltech.edu (E.S. Sosa).
[1] Now at Division of Earth and Climate Sciences, Duke University, Durham, North Carolina 27708.

1. Introduction

Iron isotope variations in lavas and mantle rocks are effective tracers of differentiation (Sossi et al., 2012; Nebel et al., 2015; Williams et al., 2018), partial melting (Weyer and Ionov, 2007; Williams and Bizimis, 2014), and changes in oxygen fugacity (fO_2) (Williams et al., 2005; Dauphas et al., 2014). The utility of Fe isotopes (expressed in delta notation as $\delta^{56}Fe = 1000 \times [(^{56}Fe/^{54}Fe)_{sample}/(^{56}Fe/^{54}Fe)_{standard} -1)]$ in understanding these processes largely reflects the respective affinities of isotopically light versus heavy Fe for reduced (Fe^{2+}) and oxidized (Fe^{3+}) valence states (Polyakov and Mineev, 2000). Due to the oxidized nature of arc lavas (up to 3 log units above the fayalite-magnetite-quartz redox buffer [FMQ]) relative to mid-ocean ridge basalts (MORB: ~FMQ) (e.g., Cottrell et al., 2021, and references therein), and the preference for isotopically heavy Fe species in oxidized magmas (Dauphas et al., 2009, 2014; Roskosz et al., 2023), arc magmas are theoretically expected to display higher $\delta^{56}Fe$ than MORB. However, the Fe isotope compositions of arc lavas show more variability and extend to isotopically lighter values than the observed range in MORB (arcs: $\delta^{56}Fe$ = –0.09 to +0.20 ‰, Dauphas et al., 2009; Foden et al., 2018; Williams et al., 2018; Chen et al., 2023; as compared to MORB: $\delta^{56}Fe$ = +0.06 to +0.18 ‰, Weyer and Ionov, 2007; Teng et al., 2013) (Fig. 1a).

The greater variability in $\delta^{56}Fe$ and the presence of isotopically light compositions in arc lavas may reflect a combination of several processes that distinctively operate in subduction zones, including (1) greater depletion in some arc sources due to higher extents of wet melting (e.g., Nebel et al., 2015; Foden et al., 2018; Chen et al., 2021), (2) reaction between subarc mantle peridotite and isotopically variable fluid fluxes from the subducted slab (Nebel et al., 2013; Debret et al., 2016; Deng et al., 2022; Chen et al., 2023), or (3) the effects of lower to mid-crustal differentiation in arcs (Li et al., 2020; Cooper and Inglis, 2022; Du et al., 2022). For example, subarc mantle peridotites are also isotopically light relative to those from mid-ocean ridges (Fig. 1b and references therein), which may reflect prior melt depletion of the subarc mantle (Williams et al., 2005; Williams and Bizimis, 2014) or metasomatism by isotopically light fluids derived from serpentinite breakdown in the slab (Debret et al., 2016, 2018, 2020). The latter process would suggest that the $\delta^{56}Fe$ of arc magmas may be inherited from their sources. In contrast, Foden et al. (2018) observed negative correlations between arc thermal parameter (φ, an expression of the slab temperature profile) and $\delta^{56}Fe$ in a globally distributed suite of mafic arc lavas, suggesting that light Fe isotope compositions in convergent margin magmas may instead reflect greater extents of flux melting in arcs with older and colder subducting slabs. This would imply that the isotopic depletion in some arc magmas reflects not only variable degrees of alteration of the mantle source but also differences in geodynamic regime.

In concert with the above processes, magmatic differentiation may also play an important role in the Fe isotope evolution of arc magmas due to the differences in bond strength between fractionating minerals (including silicates, oxides, and sulfides) and the melt (Dauphas et al., 2014; Sossi and O'Neill, 2017). Isotopically heavy Fe is preferentially incorporated into Fe^{3+}-bearing phases (e.g., oxides such as magnetite) over Fe^{2+}-bearing phases (e.g., olivine, orthopyroxene, garnet, and sulfides). The effects of magmatic differentiation on Fe isotope systematics in arcs have primarily been studied through the volcanic record (Nebel et al., 2015; He et al., 2017; Foden et al., 2018; Williams et al., 2018; Johnson et al., 2023). For example, Williams et al. (2018) found that producing the major/trace element and Fe isotope trajectories ($\delta^{56}Fe$ = –0.04 to +0.09 ‰) of basaltic to dacitic lavas from Anatahan volcano (Marianas) requires three distinct stages with different crystallizing assemblages, including (1) olivine and pyroxene, (2) magnetite, and (3) sulfide fractionation. In comparison to the Marianas, which are built on relatively thin crust (~20 km; Calvert et al., 2008), the Fe isotope compositions of lavas from the Central Andes have higher $\delta^{56}Fe$ ($+0.14 \pm 0.04$ ‰) and Sm/Yb (Du et al., 2022). This may suggest that early garnet fractionation at the base of the thick Andean crust (~60 km)
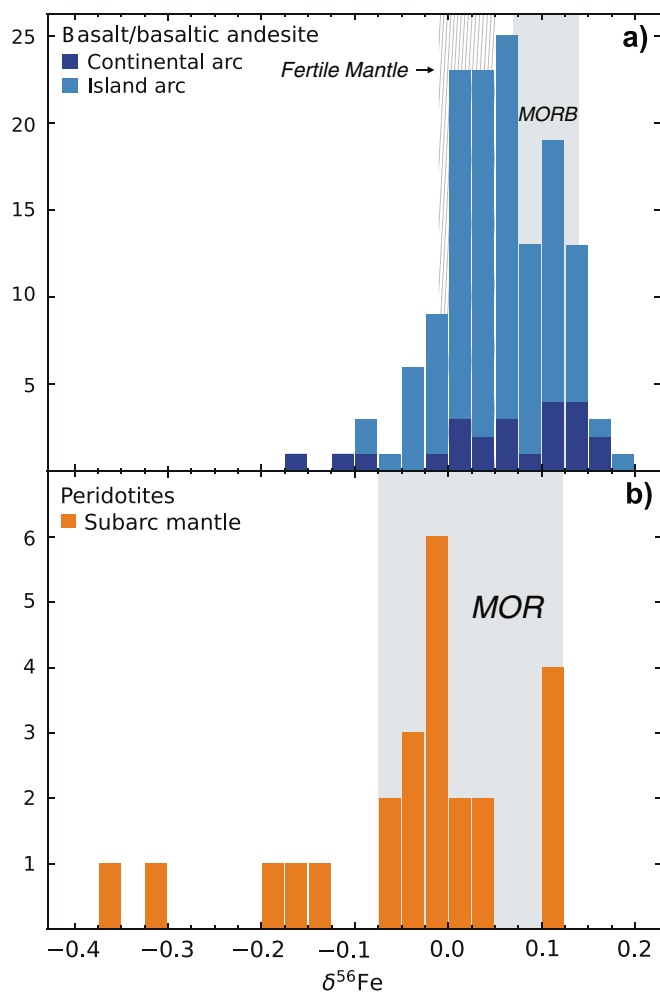

Fig. 1. Frequency histograms of $\delta^{56}Fe$ (‰) in (a) arc basalts and basaltic andesites and (b) subarc mantle peridotites show the observed range in Fe isotope compositions for both rock types and how arc lavas and mantle rocks extend to more depleted compositions than observed in those from MOR environments. Arc lava data is from Dauphas et al. (2009), Foden et al. (2018), Williams et al. (2018), Du et al. (2022), and Chen et al. (2023). Subarc mantle peridotite data is from Williams et al. (2005), Poitrasson et al. (2013), Weyer and Ionov (2007), and Turner et al. (2018). MORB field (gray in panel a) is from Teng et al. (2013) and fertile upper mantle field (hatched lines) is from Weyer and Ionov (2007). MOR peridotite data (panel b) is from Craddock et al. (2013).

drove later-stage melts to heavier Fe isotope compositions (Du et al., 2022). However, in a recent study of Indonesian calc-alkaline lavas, Johnson et al. (2023) found no correlations between indices of fractionation (e.g., SiO_2 and MgO) and $\delta^{56}Fe$. This led the authors to suggest that $\delta^{56}Fe$ of the melt was buffered by the crystallization of isotopically heavy magnetite, which prevented late-stage magmas from acquiring heavy Fe isotope compositions (Johnson et al., 2023). Taken together, these studies suggest that fractional crystallization may have variable effects on the Fe isotope evolution of magmas depending on the crystallizing assemblage and P-T-fO_2-H_2O conditions.

The plutonic record of differentiation in arcs and its effect on Fe isotope systematics in evolving melts has received comparatively less attention. Li et al. (2020) measured the Fe isotope compositions of gabbro and diorite samples from the Tongde region of Southern China. These rocks display an initial period of modest isotopic enrichment followed by a decrease in $\delta^{56}Fe$ as fractionation progresses, a pattern which Li et al. (2020) attribute to the removal of isotopically light garnet, pyroxene, and olivine in a deep crustal hot zone followed by crystallization of isotopically heavy amphibole at mid-crustal levels.

Cooper and Inglis (2022) found that mid to upper-crustal (≤0.4 GPa) gabbro, gabbronorite, and hornblendite cumulate xenoliths from the Lesser Antilles had higher $\delta^{56}Fe$ compositions than upper-crustal non-cumulate gabbro xenoliths and erupted lavas, suggesting that mid-crustal fractionation depleted the melt in the heavy isotopes of Fe. However, this cumulate suite was restricted to mid to upper-crustal samples (≤15 km; Cooper et al., 2016, 2019) and did not include lower crustal ultramafic assemblages (MgO < 13.4 wt% for all samples analyzed).

Understanding the source of the Fe isotope variability in arc lavas requires constraining the nature of primitive arc melts and how their $\delta^{56}Fe$ evolves during ascent through the entire crustal column. To address this, we measured Fe isotope compositions in ultramafic to mafic cumulate (*n* = 28) and mantle (*n* = 1) xenoliths from a well-documented lower to mid-crustal xenolith suite from the Adagdak Volcano on Adak Island, Central Aleutians (Fig. 2) (Debari et al., 1987; Sosa et al., 2023). We analyzed both minerals (spinel, clinopyroxene, olivine, amphibole, and magnetite) and whole-rock Fe isotope ratios. Amphibole Fe isotope data are complemented by single-crystal synchrotron Mössbauer spectroscopy of two amphibole grains, one from an amphibole gabbro (sample ADG-CB-1) and the other from a hornblendite (sample ADG-82-18). These measurements allow us to determine $Fe^{3+}/\Sigma Fe$ ratios for these grains and evaluate the potential of amphibole to drive the Fe isotopic evolution of Adagdak melts.

Our data extend to more primitive compositions than reported in the previous study of cumulate xenoliths (Cooper and Inglis, 2022), capturing a different, but complementary, interval of fractional crystallization (Fig. 3). We also measured $\delta^{56}Fe$ for five lavas from Mt. Adagdak, ranging from basalt to andesite (Kay and Kay, 1985, 1990, 1994). With this data, we construct a model to explore the effects of fractional crystallization of the isotopic evolution of arc magmas. Our results show that the cumulates chronicle a complex isotopic history that is not captured in the lava record.

2. Geological background and sample descriptions

The Aleutian oceanic arc spans approximately 2000 km, extending from the western edges of the Alaskan Peninsula to its western terminus at the Kamchatka Peninsula. The arc consists of a largely submarine intra-oceanic ridge, which is only subaerial at volcanic centers (e.g., Scholl et al., 1975; Kay and Kay, 1994). Magmatism results from the northward subduction of the Pacific plate beneath the North American plate (e.g., Jicha and Kay, 2018). Although the arc has migrated northward since 40 Ma, active magmatism in the Aleutians has occurred in a geometry similar to that of the present day for the past 52 to 46 million years (e.g., Kay et al., 1982, 1994; Davis et al., 1989; Jicha et al., 2006; Jicha and Kay, 2018). Crustal thicknesses show little variability and are approximately 39 ± 3 km all along the arc (Janiszewski et al., 2013). The xenolith suite from Mount Adagdak on Adak Island in the central Aleutians was collected in the late 1970 s on the volcano's western slope from an olivine-phyric basalt flow (Fig. 2) (Debari et al., 1987). While the age of the Adagdak xenolith suite is unknown, exposed plutonic rocks on Adak Island have been dated from ~ 14 to 38 Ma (Citron et al., 1980; Jicha et al., 2006; Kay et al., 2019). The petrography, mineral chemistry, and crystallization conditions of the xenolith suite are extensively described in Debari et al. (1987) and Sosa et al. (2023), but we briefly highlight the most salient features here.

The samples described here were taken in 2017 from the Cornell collection, which includes extensive xenolith suites from both Mount Adagdak and Mount Moffett on Adak Island. The Adagdak xenolith suite is comprised of lower to mid-crustal cumulates, which range from primitive spinel dunite and wehrlite to more evolved amphibole gabbro and hornblendite. The crystallization sequence for the Adagdak cumulate suite is inferred to be olivine + clinopyroxene + spinel → clinopyroxene + amphibole + plagioclase + magnetite. The elongate and
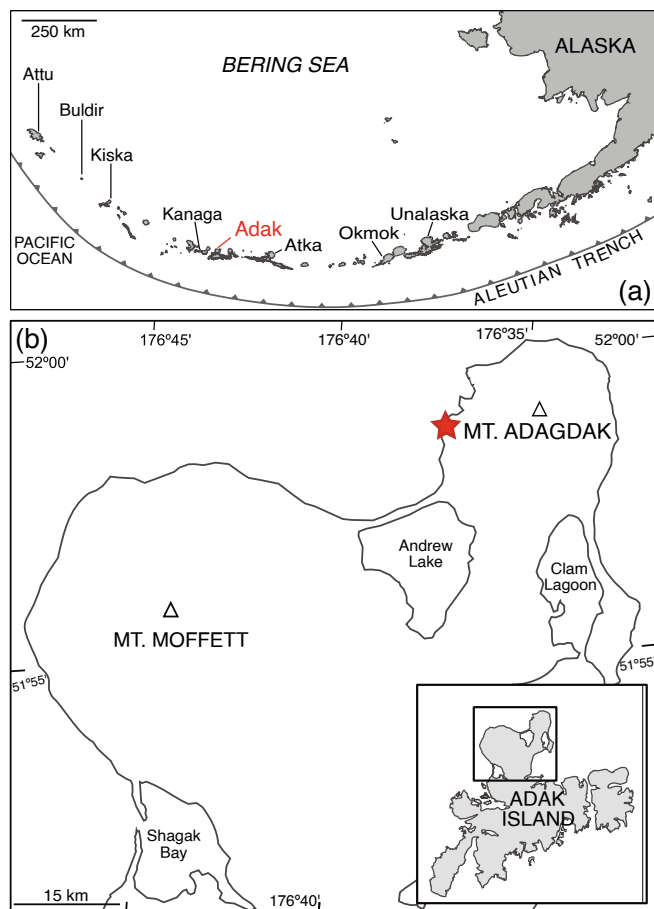
Fig. 2. Simplified map of the Aleutian Arc (a) with enlargement of Adak Island (b). The location where the Mount Adagdak xenolith suite was collected from (51°58.78′ N, 176°37.36′ W) is designated with a red star. Modified from Sosa et al. (2023).
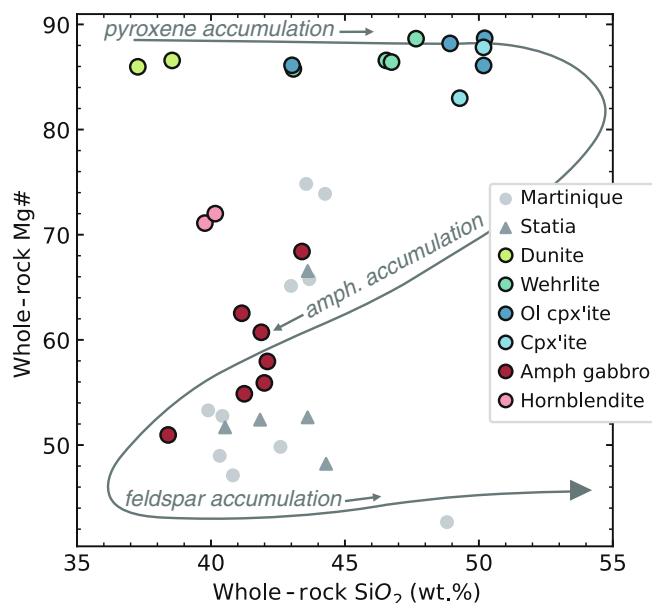
Fig. 3. SiO$_2$ vs Mg# for whole-rock cumulate xenolith compositions from Martinique and Statia (Lesser Antilles; Cooper and Inglis, 2022) and Adagdak. Gray curve represents the experimental cumulate trend of hydrous arc basalts from Müntener and Ulmer (2018).

euhedral character of amphibole in the amphibole gabbro and hornblendite samples suggests a cumulate rather than peritectic origin (Debari et al., 1987; Sosa et al., 2023). peritectic amphibole is only observed as thin veins (<1 % by volume) along clinopyroxene grain boundaries in (±olivine) clinopyroxenite xenoliths (Sosa et al., 2023). The only oxide phase in the ultramafic cumulates is Fe-Cr-Al-Mg spinel (hitherto referred to simply as "spinel"), while the amphibole gabbro and hornblendite lithologies contain magnetite. The suite also contains one mantle lherzolite. Olivine-spinel-pyroxene oxybarometry of the ultramafic lithologies yields oxygen fugacity estimates of ΔFMQ = +0.1 to +2.1. Thermobarometry yields temperatures between 950 and 1150 °C for the ultramafic lithologies and 920 to 1070 °C for the amphibole gabbro and hornblendite samples (Sosa et al., 2023). The dunite, wehrlite, and clinopyroxenite xenoliths display adcumulate textures, whereas the amphibole gabbro and hornblendite samples have mesocumulate to orthocumulate textures. Based on mineral chemistry, amphibole-only geobarometry, and comparisons to experimental studies, Sosa et al. (2023) interpreted the ultramafic assemblages (dunite and wehrlite cumulates) to be lower-crustal in origin, while the more evolved amphibole gabbro and hornblendite cumulates are likely sourced from the middle crust.

For this study, Fe isotope ratios were measured on whole-rock powders and/or mineral separates for 29 xenolith samples. These xenolith include dunite ($n = 3$), wehrlite ($n = 8$), olivine clinopyroxenite ($n = 5$), clinopyroxenite ($n = 2$), amphibole gabbro ($n = 7$), and hornblendite ($n = 3$) cumulates and one mantle xenolith, which is distinguished from the cumulate samples by highly magnesian olivine (Mg# = 91.3) $100 \times [Mg/(Mg + Fe^T)]$ molar), clinopyroxene (Mg# = 93.8), and orthopyroxene (Mg# = 92.2) and chromium-rich spinel (Cr# = 60.0: where Cr# = $100 \times Cr/[Cr + Al]$ molar) (Sosa et al., 2023). Representative photomicrographs and modal mineral proportions of thin sections for selected samples are given in the Supplemental Data (Figs. S1 and S2, Table S1), Sosa et al. (2023), and Debari et al. (1987). We also measured Fe isotope compositions of 5 lavas from Mt. Adagdak, which range from basalt to andesite (Supplemental Data, Table S7; Kay and Kay, 1985; 1994). Note that none of these samples represent the magnesium-rich host lava for the xenolith suite (Debari et al., 1987), but rather a more typical array of magma compositions erupted from Mt. Adagdak.

3. Materials and methods

3.1. Bulk-rock analyses

Samples were selected for bulk-rock analysis based both on grain size and the overall xenolith dimensions to ensure a representative measurement. Samples were cut into smaller aliquots (40–70 g per aliquot) to remove altered surfaces or veining. Samples were then polished with sandpaper to remove any saw marks and sonicated in deionized water. Cleaned aliquots were crushed and powdered in an agate grinding vessel. Powders were dried overnight at 110 °C, then heated to 1050 °C for one hour to determine loss on ignition (LOI). The LOI for amphibole-rich samples ($n = 9$) was performed at 1100 °C to ensure any structurally bound water was volatilized. Glass beads were prepared using a 10:1 mass ratio of Li-borate flux to sample powder and fused at 1200 °C. Major elements (Si, Ti, Al, Fe, Mn, Mg, Ca, Na, K, P) were analyzed using a Panalytical Zetium 4 kW wavelength-dispersive X-ray fluorescence (XRF) spectrometer at Caltech following methods in Bucholz and Spencer (2019). Trace elements (Cr, Ni, Rb, Sr, Y, Zr, Ba, Nb, Cs, all REEs, Hf, Ta, Pb, Th, U) were measured from glass chips of the Li-borate beads through solution inductively-coupled plasma mass spectrometry following methods described in Lewis et al. (2021). Bulk-rock xenolith compositions ($n = 19$) are given in the Supplemental Data (Table S2).

3.2. Mineral chemistry

Major element mineral compositions of olivine, clinopyroxene, amphibole, and magnetite were obtained from polished thin sections with a JEOL JXA-8200 Electron Probe MicroAnalyzer (EPMA) at Caltech. These analyses were combined with previously obtained major and trace element mineral compositions for the cumulate xenoliths (Sosa et al., 2023). The majority of the mineral major element data used in this study and all of the trace element data were presented in Sosa et al. (2023), which details the analytical conditions, detection limits, and data reduction of these analyses. The same analytical conditions and data reduction procedures were used here. All mineral data are provided in the Supplemental Data (Table S3-S6) along with the corresponding Fe isotope analyses, and the source of the major element data (i.e., Sosa et al., 2023 vs. this study) is noted for each analysis in the Supplemental Data. The most salient features of these data are highlighted in Table 1.

3.3. Single-crystal Mössbauer spectroscopy

Single-crystal synchrotron Mössbauer spectroscopy (SMS) of amphibole grains ($n = 2$) was performed at the Advanced Photon Source, Argonne National Laboratory, USA, following the methodology described in Ratschbacher et al. (2023). Both amphibole grains were fully characterized through EPMA (major and minor elements), secondary-ion mass spectrometry (SIMS) to determine water contents and hydrogen isotope composition, and single crystal-X-ray diffraction to determine unit cell parameters and identify twinning prior to SMS. Details of these analyses are given in the Supplemental Data. Single-crystal time-domain Mössbauer spectra were collected at beamline 3ID-D during the hybrid mode filling pattern of the storage ring. For each grain, spectra were collected in two distinct crystallographic orientations with and without a stainless-steel reference foil (natural isotopic abundance of ^{57}Fe; thickness of 10 µm). Spectra were fitted using the CONUSS 2.3.0 software package (Sturhahn, 2000; 2021). Additional details related to the SMS experiments and the spectral fitting results—including the time window used to fit the spectra, the best-fit hyperfine parameters and their uncertainties, as well as the Euler angles and asymmetry parameters determined from the "K-H" hornblende crystal structure reported in Makino and Tomita (1989)—are given in the Supplemental Data.

3.4. Iron isotopes

The Fe isotopic composition of mineral separates and whole-rock powders were measured at the Isotoparium, Caltech. Mineral separates were hand-picked using stainless steel tweezers under a binocular to ensure all grains were free of inclusions and visible alteration. Grains were then sonicated in isopropyl alcohol and deionized water to remove any surface contamination. Reference USGS rock powders AGV-2, BHVO-2, BCR-2, and COQ-1, whose Fe isotope compositions have previously been measured (Craddock and Dauphas (2011)), were prepared and analyzed alongside samples to confirm data accuracy. Sample digestion and Fe separation via ion chromatography followed the methods of Dauphas et al. (2004). Across all repeated analyses, USGS rock powders AGV-2, BHVO-2, BCR-2, and COQ-1 yielded average $\delta^{56}Fe$ of + 0.100 ± 0.007, +0.113 ± 0.010, +0.104 ± 0.008, and –0.095 ± 0.026 ‰, respectively, in agreement with previously published values for these samples (AGV-2 = +0.105 ± 0.011 ‰, BHVO-2 = +0.114 ± 0.011 ‰, BCR-2 = +0.091 ± 0.011 ‰, and COQ-1 = –0.117 ± 0.030 ‰: Craddock and Dauphas (2011)). The measured Fe isotope ratios for each replicate analysis of the USGS standard powders are given in the Supplemental Data (Table S8). The measured compositions of these reference rock powders show long-term reproducibility from January to December of 2022 (Supplemental Data, Table S8).

Whole-rock powders (1–2 mg) and mineral separates of olivine (1–2 mg), clinopyroxene (2–3 mg), amphibole (1–2 mg), and magnetite (~1

Table 1
Fe isotope compositions and select major element data for Adagdak samples.

Sample	Phase	Fe isotope data (‰)					Major element data (wt.%)		
		n	$\delta^{56}Fe$	Err	$\delta^{57}Fe$	Err	MgO	FeO$_T$	Mg#
Amphibole gabbro									
ADG-38	Whole rock	6	0.076	0.043	0.116	0.068	7.23	9.35	57.95
	Magnetite	10	0.107	0.017	0.159	0.027	2.93	79.76	14.01
ADG-74	Whole rock	8	0.041	0.044	0.070	0.069	7.30	8.42	60.72
	Clinopyroxene	6	0.050	0.025	0.078	0.041	12.28	8.27	72.58
	Magnetite	7	0.112	0.015	0.162	0.028	2.98	79.78	14.15
ADG-4	Whole rock	8	0.064	0.033	0.083	0.046	7.35	10.77	54.87
ADG-73	Whole rock	7	0.057	0.018	0.073	0.032	7.84	11.03	55.91
	Magnetite	6	0.125	0.028	0.191	0.051	2.79	80.50	13.25
ADG-82-5	Whole rock	8	0.065	0.050	0.090	0.074	8.04	13.79	50.96
ADG-6	Whole rock	8	0.056	0.033	0.093	0.046	9.67	10.32	62.53
	Clinopyroxene	7	0.072	0.025	0.100	0.041	13.24	8.27	74.04
	Amphibole	7	0.065	0.039	0.100	0.053	12.71	12.38	64.68
ADG-CB-1	Whole rock	6	0.059	0.025	0.085	0.045	13.73	11.31	68.40
	Clinopyroxene	6	0.067	0.025	0.099	0.045	13.40	7.64	75.26
	Amphibole	7	0.076	0.021	0.110	0.048	13.81	11.03	69.03
Hornblendite									
ADG-26	Whole rock	6	0.077	0.025	0.104	0.041	14.21	10.29	71.10
ADG-82-18	Whole rock	6	0.074	0.025	0.114	0.045	14.47	10.03	72.00
	Amphibole	7	0.089	0.028	0.123	0.041	13.92	10.11	71.04
ADG-52	Amphibole	6	0.067	0.028	0.101	0.041	13.23	10.47	67.62
Clinopyroxenite									
ADG-82-1	Whole rock	7	0.085	0.018	0.138	0.032	15.21	5.56	82.98
ADG-82-15	Whole rock	8	0.049	0.050	0.074	0.074	17.27	4.27	87.82
	Clinopyroxene	6	0.090	0.038	0.140	0.067	15.52	4.05	87.20
Olivine clinopyroxenite									
ADG-8	Whole rock	8	0.035	0.037	0.059	0.061	16.41	4.72	86.10
	Whole rock*		0.050	0.054	0.072	0.077	19.44	4.79	87.85
	Olivine	9	−0.019	0.037	−0.023	0.053	46.50	12.38	87.00
	Clinopyroxene	7	0.083	0.035	0.115	0.056	15.36	4.84	84.99

Sample	Phase	Fe isotope data (‰)					Major element data (wt.%)		
		n	$\delta^{56}Fe$	Err	$\delta^{57}Fe$	Err	MgO	FeO$_T$	Mg#
ADG-DR	Whole rock	8	0.046	0.037	0.090	0.061	19.47	4.43	88.68
	Whole rock*		0.039	0.056	0.057	0.072	20.49	4.42	89.21
	Olivine	9	−0.015	0.043	−0.023	0.046	46.13	13.50	85.90
	Clinopyroxene	7	0.077	0.035	0.113	0.056	16.22	3.86	88.23
ADG-CB-7	Olivine	9	−0.003	0.043	0.015	0.067	45.78	13.20	86.08
	Clinopyroxene	6	0.058	0.038	0.099	0.067	15.99	3.78	88.23
ADG-32	Olivine	5	−0.086	0.023	−0.129	0.040	46.44	12.84	86.64
	Clinopyroxene	8	−0.012	0.031	−0.019	0.043	15.93	3.75	88.18
ADG-82-17	Whole rock	8	−0.036	0.037	−0.049	0.061	34.72	9.98	86.11
	Whole rock*		−0.010	0.055	−0.001	0.090	34.84	9.60	86.61
	Olivine	7	−0.016	0.040	−0.006	0.060	45.58	13.70	85.57
	Clinopyroxene	6	0.033	0.038	0.048	0.067	16.05	3.86	88.15
ADG-CB-8	Olivine	9	0.004	0.037	0.003	0.053	45.86	14.11	85.28
	Clinopyroxene	5	0.108	0.018	0.160	0.034	15.85	4.16	87.17
Wehrlite									
ADG-82-3	Whole rock	6	0.065	0.039	0.129	0.053	26.40	6.03	88.64
ADG-CB-5	Olivine	8	−0.099	0.030	−0.132	0.051	44.38	15.01	84.06
	Clinopyroxene	8	−0.051	0.030	−0.069	0.051	15.84	4.43	86.45
ADG-33	Olivine	6	−0.007	0.044	−0.017	0.065	45.48	13.97	85.30
	Clinopyroxene	8	0.089	0.031	0.127	0.043	15.90	4.06	87.48
ADG-10	Olivine	8	−0.024	0.033	−0.038	0.046	45.31	13.83	85.38
	Clinopyroxene	8	0.027	0.030	0.066	0.051	15.94	4.07	87.77
ADG-35	Olivine	7	0.032	0.035	0.041	0.056	45.40	13.63	85.59
	Clinopyroxene	7	0.082	0.019	0.113	0.030	15.63	3.77	87.96
	Spinel (vial 18)	7	0.212	0.017	0.302	0.034	13.63	15.82	60.56
	Spinel (vial 5)	6	0.264	0.040	0.394	0.064	13.63	15.82	60.56
ADG-42	Whole rock	8	−0.043	0.050	−0.060	0.074	32.14	9.51	85.77
	Whole rock*		0.014	0.053	0.019	0.082	27.86	10.1	83.61
	Olivine	8	−0.024	0.031	−0.034	0.043	45.51	13.88	85.39
	Clinopyroxene	7	0.035	0.040	0.048	0.060	16.07	3.75	88.42
	Spinel (vial 16)	7	0.097	0.017	0.137	0.034	11.57	17.41	54.23

Sample	Phase	Fe isotope data (‰)					Major element data (wt.%)		
		n	$\delta^{56}Fe$	Err	$\delta^{57}Fe$	Err	MgO	FeO$_T$	Mg#

Table 1 (*continued*)

ADG-30	Clinopyroxene	8	0.075	0.030	0.141	0.051	15.58	3.75	88.09
	Olivine	8	0.023	0.035	0.027	0.056	45.51	13.62	85.64
	Spinel (vial 13)	5	0.266	0.032	0.417	0.045	13.36	16.24	59.47
Cumulate dunite									
ADG-82-21	Whole rock	8	−0.094	0.044	−0.138	0.069	44.47	12.29	86.57
	Olivine	6	−0.077	0.038	−0.121	0.067	46.08	12.21	87.05
	Spinel (vial 11)	7	0.208	0.018	0.324	0.031	13.07	15.61	59.88
ADG-63	Olivine	6	0.065	0.018	0.101	0.027	46.24	12.32	86.95
	Spinel (vial 2)	5	0.279	0.032	0.416	0.045	14.39	14.86	63.31
	Spinel (vial 14)	6	0.264	0.019	0.401	0.035	14.39	14.86	63.31
ADG-82-2	Whole rock	8	−0.017	0.033	−0.042	0.046	45.89	13.35	85.97
	Spinel (vial 8)	6	0.234	0.029	0.362	0.041	12.63	15.96	58.53
	Spinel (vial 9)	6	0.223	0.040	0.334	0.064	12.63	15.96	58.53
Mantle dunite									
ADG-CB-9	Whole rock	8	−0.034	0.049	−0.055	0.072	48.95	9.13	90.52
	Spinel (vial 12)	6	0.109	0.020	0.167	0.033	13.88	12.85	65.83
	Spinel (vial 7)	6	0.176	0.040	0.284	0.064	13.88	12.85	65.83
Lava									
ADAG-81-4	Whole rock	6	0.062	0.017	0.078	0.028	5.68	10.27	49.65
ADAG-81-2	Whole rock	6	0.041	0.015	0.066	0.022	2.45	6.78	39.18
ADAG-81-8	Whole rock	7	0.031	0.015	0.050	0.028	2.53	6.00	42.91
ADAG-81-7A	Whole rock	6	0.048	0.027	0.073	0.053	4.79	9.62	47.02
ADAG-81-7	Whole rock	6	0.047	0.027	0.071	0.053	3.30	7.96	42.50

*Whole rock values calculated from $\delta^{56}Fe$ of all Fe-bearing phases based on mineral modes, densities, and major element chemistry.

mg) were digested using a series of acid attacks on hot plates: (1) 1.5 mL concentrated 2:1 $HF:HNO_3$ solution for 5 h at 100 °C, (2) 1.25 mL of 3:1 $HCl:HNO_3$ (aqua regia) overnight at 140 °C, (3) 1.5 mL of 2:1 $HCl:HNO_3$ overnight at 140 °C, (4) 1 mL concentrated HCl at 180 °C for two days. Samples were fully dried between each digestion step. After the final digestion, samples were dried, brought into a 6 M HCl solution, and refluxed overnight at 130 °C in preparation for column chemistry. We were not able to digest bulk spinel mineral separates using the methods presented above due to spinel's refractory nature, and instead opted to digest, chemically purify, and analyze single grains of spinel. Each spinel grain was individually digested in a Parr bomb for a total of eight days. First, each spinel grain was loaded into a separate 200 μL microcapsule and digested in three drops (~90 μL) of concentrated HF inside a Parr bomb for two days at 210 °C. While remaining inside the microcapsule, the spinel grains were then dried down on a hot plate, taken back into solution with three drops of 5 M HCl, and refluxed in the Parr bomb at 180 °C for two days. Each spinel grain went through an additional round of digestion, first in concentrated HF then (after being dried down again) in 5 M HCl, before being fully dried and brought into a 6 M HCl solution prior to column chemistry.

Iron purification was performed using 10 mL polyethylene chromatography columns (Biorad Polyprep) with 1 mL of BioRad AG1-X8 (200–400 mesh size) anion exchange resin. The samples were loaded in 0.5 ml of 6 M HCl. Matrix elements were eluted with 9 mL of 6 M HCl, and the purified Fe cut was then recovered with 8 mL of 0.4 M HCl. To ensure complete removal of all matrix-forming elements, column chemistry was performed twice for each sample. In preparation for analysis, samples were dried down and refluxed overnight at 140 °C in 0.5 mL of concentrated HNO_3. Samples were then dried to a drop (<25 μL), taken back up in 5 mL of 0.3 M HNO_3 run acid, and refluxed overnight at 130 °C.

Iron isotope measurements were made on a Neptune Plus (Thermo-Fisher) Multi-Collector Inductively-Coupled-Plasma Mass-Spectrometer (MC-ICP-MS) in wet plasma conditions (glass spray chamber). To resolve ArO interferences, measurements were performed in high mass resolution mode using ThermoFisher general Ni sample and skimmer cones and a static cup configuration monitoring masses 53 through 60. In addition to all four isotopes of Fe, we also measured ^{53}Cr, ^{55}Mn, ^{59}Co, and ^{60}Ni. Measurements of ^{53}Cr and ^{60}Ni were respectively used to account for and remove interferences of ^{54}Cr on ^{54}Fe and ^{58}Ni on ^{58}Fe,

while ^{55}Mn and ^{59}Co were monitored to verify complete separation of Fe from matrix elements during column chemistry. All Faraday cups were assigned 10^{11} Ω feedback resistors, except for ^{60}Ni (H4 cup), which was assigned a 10^{12} Ω feedback resistor to improve the accuracy of Ni isobaric interference monitoring and corrections. Cup gains were calibrated at least weekly, and the instrument was tuned for optimal sensitivity and stability.

Standard and sample solutions diluted to a final Fe concentration of 5 μg/g in 3 % vol HNO_3 were aspired using a PFA nebulizer with a nominal flow rate of 50 μl/min, yielding a typical beam intensity of 20–25 V on ^{56}Fe, corresponding to a sensitivity of 4–5 V/ppm. On-peak-zeros (OPZ) were measured before all samples and standards using a 90 s uptake and 40 s of on-peak measurement of clean acid solution from the same batch used to dilute the samples. This was done to monitor memory effects of the sample introduction system and remove background from all measurements. Typical background intensities were ~ 5–7 mV on ^{56}Fe. Sample and bracketing standard measurements consisted of 90 s of sample uptake, followed by 50 cycles of 4.192 s integration time for each measurement, for a total of 210 s of static on-peak sample measurement. The inlet system was then rinsed for 120 s between samples using 3 % vol HNO_3, before repeating the cycle for the next standard/unknown. Each unknown measurement was bracketed with the IRMM-524b metallic Fe standard diluted in the same run acid and at the same Fe concentration (within 5 %). Within each run, at least one USGS reference material was measured alongside the unknown samples.

Following the methods of Dauphas et al. (2009), we calculated the corresponding error for each measurement using the standard deviation (SD) of the IRMM-524b standard for each analytical session:

$$Error = 2*SD_{IRMM-524b}/\left(n_{sample}\right)^{0.5}$$

where n_{sample} is the number of measurements performed for the sample. During standard bracketing, the IRMM-524b standard is measured more frequently than any one sample, and its standard deviation is therefore taken to be more representative of the actual uncertainty for the analytical session (Dauphas et al., 2009).

4. Results

4.1. Xenoliths

4.1.1. Whole-rock

The cumulate compositions display the characteristic Z-shaped pattern on a Mg# versus SiO_2 diagram that is typical for cumulates formed from the differentiation of hydrous, oxidized arc magmas (e.g., Müntener and Ulmer, 2018; Fig. 3). Silica concentrations (37.4–50.0 wt % for all samples) are lowest in the dunite samples (37.4–38.7 wt%) and increase to 49–50 wt% in the clinopyroxenite xenoliths at a relatively constant Mg# (83–89) (Fig. 3). Amphibole accumulation then leads to a decrease in Mg# (51–72) and SiO_2 (43 wt%) for both hornblendite and amphibole gabbro xenoliths. MgO varies from 7.2 to 45.9 wt% for the

cumulate xenoliths, while mantle xenolith ADG-CB-9 has 49.0 wt% MgO (Fig. 4a). FeO_T ranges from 4.3 to 13.8 wt% in the cumulate samples, with the lowest values observed in the ($\pm$olivine) clinopyroxenite xenoliths (4.3–5.6 wt%). The one analyzed mantle xenolith has a Mg# of 90.5 and 38.6 wt% SiO_2.

While thin section petrography of sample ADG-CB-9 indicated that the sample should be classified as a lherzolite (albeit at the lherzolite-dunite boundary on the IUGS ultramafic classification diagram), the high whole-rock MgO content of this sample suggests that in a bulk-rock content, this sample should be classified as a dunite. To estimate modal abundances for the dunite sample, we used mineral compositions, our whole-rock chemistry, and the Log-ratio Inversion of Mixed End-members (LIME) model of Prissel et al. (2023) to balance our whole-rock data against the average compositions of measured mineral
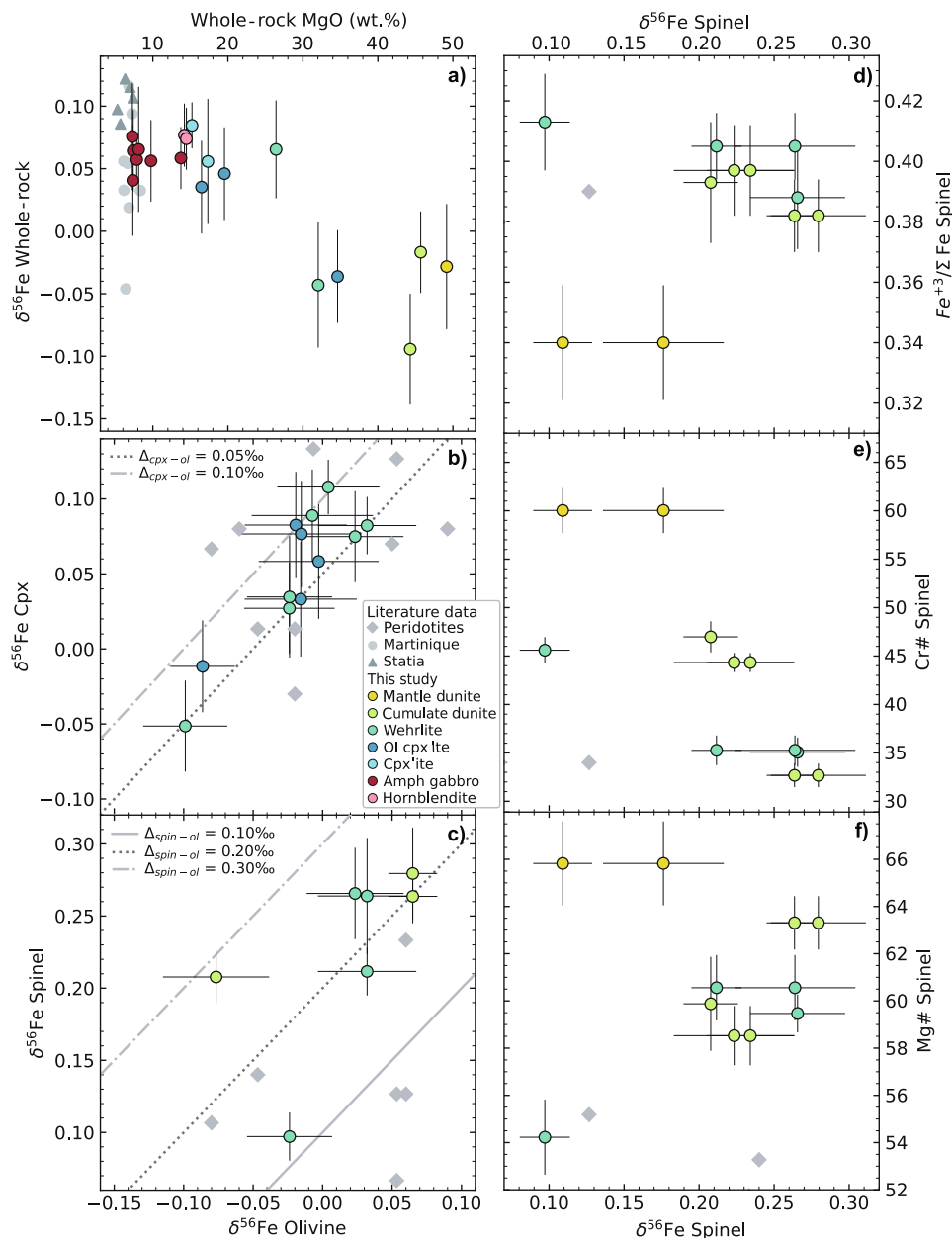

Fig. 4. Adagdak xenoliths whole-rock and mineral chemistry vs. Fe isotope ratios. (a) Whole-rock δ^{56}Fe (‰) vs. MgO (wt.%). (b) δ^{56}Fe cpx vs. δ^{56}Fe of coexisting olivine. Grey dashed and dotted lines represent olivine-clinopyroxene fractionation for $\Delta^{56}Fe_{cpx-ol}$ of 0.05 and 0.10 ‰, respectively. (c) δ^{56}Fe spinel vs. δ^{56}Fe of coexisting olivine. Grey dashed, dotted, and solid lines represent spinel-olivine fractionation for $\Delta^{56}Fe_{spin-ol}$ of 0.10, 0.20, and 0.30‰, respectively. (d) δ^{56}Fe spinel vs. Fe^{3+}/ΣFe spinel. (e) δ^{56}Fe spinel vs. Cr# spinel. (f) δ^{56}Fe spinel vs. Mg# spinel. Literature data from arc mantle peridotites (Williams et al., 2005, 2014) and Lesser Antilles cumulates (Cooper and Inglis, 2022) are given for comparison.

phases. The results of these calculations suggest that the sample is, by volume, composed of approximately 96–97 % olivine, 1 % clinopyroxene, 1–2 % orthopyroxene, and 2 % spinel. This discrepancy between thin section and bulk modal proportions may be attributed to the small size of the mounted and polished thin section (~1.5 × 1.5 cm) compared to the bulk sample (~8 cm^3) and the coarse nature of the sample (grains up to 2.5 mm in diameter). As we are interested in compositional trends rather than relating Fe isotope chemistry to specific petrographic characteristics, we chose to classify this sample as a dunite for our discussion. Dunite xenoliths are therefore categorized as "cumulate dunite" (i. e., samples ADG-82-2, ADG-82-21, and ADG-63) or mantle dunite (i.e., ADG-CB-9) in all future figures, tables, and discussion.

Cumulate whole-rock Fe isotope compositions (*n* = 19) range from δ^{56}Fe = –0.09 to +0.09 ‰ and are strongly correlated to lithology and MgO (Fig. 4a) but uncorrelated with FeO$_T$. Dunite, wehrlite, and olivine clinopyroxenite cumulates with MgO > 30 wt% display the lowest δ^{56}Fe (–0.09 to +0.04 ‰), while the more evolved clinopyroxenite, hornblendite, and amphibole gabbro samples display heavier isotopic compositions (δ^{56}Fe + 0.04 to +0.09 ‰). The mantle dunite has a whole-rock δ^{56}Fe of –0.03 ± 0.05 ‰. Positive correlations are observed between whole-rock δ^{56}Fe and incompatible element concentrations (e.g., Nd, Sr; Fig. S6a, b), while compatible elements are negatively correlated with δ^{56}Fe (e.g., Cr; Fig. S6c).

4.1.2. Minerals

Olivine: Iron isotope compositions were measured for olivine separates from 14 ultramafic cumulates and range from δ^{56}Fe = –0.10 to +0.07 ‰ (Fig. 4b, c). Olivine spans a limited compositional range in terms of major elements within the cumulates (Mg# = 84–87), with no apparent correlations between olivine composition and δ^{56}Fe.

Clinopyroxene: The Fe isotope composition of clinopyroxene mineral separates (*n* = 16) from wehrlite, (±olivine) clinopyroxenite, and amphibole gabbro cumulates range from δ^{56}Fe = –0.05 to +0.11 ‰ (Fig. 4b). Clinopyroxene Mg# for these samples ranges from 72.6 to 88.2 and is highest in the ultramafic lithologies (Mg# = 85.0–88.2). Clinopyroxene δ^{56}Fe displays broad correlations with whole-rock MgO and modal mineralogy, with the highest clinopyroxene δ^{56}Fe generally observed in cpx-rich (>80 % modally) samples with whole-rock MgO between 16–20 wt%. Positive correlations are also observed between δ^{56}Fe in coexisting olivine and clinopyroxene (Fig. 4b).

Amphibole: Iron isotope compositions were measured in amphibole mineral separates from hornblendite (*n* = 2) and amphibole gabbro (*n* = 2) cumulates and range from δ^{56}Fe = +0.07 to +0.09 ‰ (Fig. 5a). Following the classification scheme of Hawthorne et al. (2012), the Adagdak cumulates contain pargasitic amphibole. Amphibole Mg# ranges from 64.7 to 71.0 for these samples. Single-crystal synchrotron Mössbauer spectra of amphibole yield Fe^{3+}/ΣFe ratios of 0.55 ± 0.06 for the grain from amphibole gabbro ADG-CB-1 (grain 6), and 0.58 ± 0.02 for the grain from hornblendite ADG-82-18 (grain 10). For ADG-CB-1 grain 6, water contents analyzed by SIMS for the same area as the SMS spectra reveal 1.60 ± 0.13 wt% H$_2$O and δD = –45 ± 11 ‰ (relative to SMOW; average of grain 6 and grain 3 from ADG-CB-1). ADG-82-18 grain 10 contains 1.34 ± 0.11 wt% H$_2$O. While we do not have D/H ratios of this grain, SIMS analyses of two other amphibole grains from
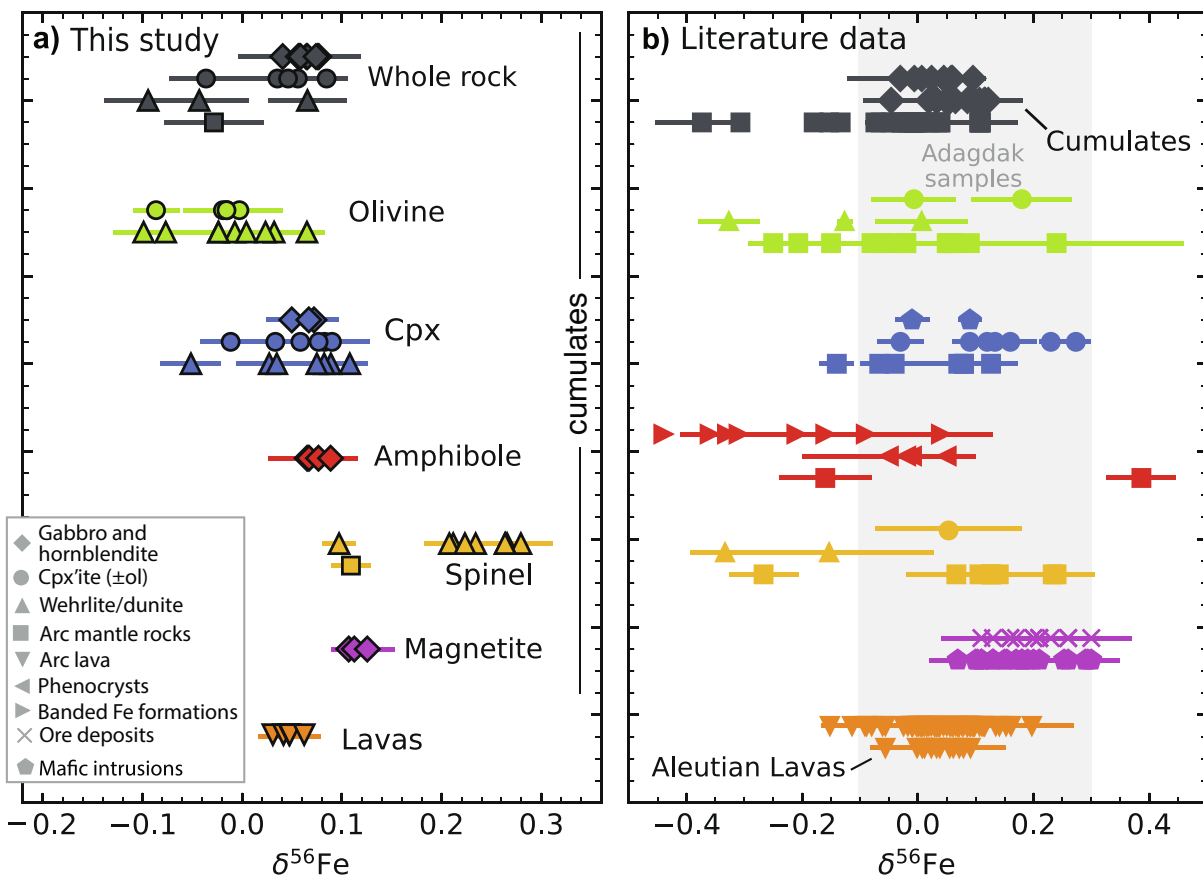

Fig. 5. Summary of Adagdak Fe isotope data and comparisons to literature data. (a) δ^{56}Fe (‰) for Adagdak whole-rock samples, lavas, and olivine, clinopyroxene, amphibole, magnetite, and single-grain spinel mineral separates. Colors distinguish between different analyzed phases and symbols differentiate specific lithologies or rock types. (b) Literature data for δ^{56}Fe of igneous rocks and minerals. Aleutian lava data is from Foden et al. (2018) and cumulate data is from Cooper and Inglis (2022; Lesser Antilles). Other literature data are from Beard et al. (2004), Williams et al., (2005,2014), Weyer and Ionov (2007), Sossi et al. (2012), Poitrasson et al. (2013), Chen et al., 2014, Zhao et al. (2015), Turner et al. (2018), Rodriguez-Mustafa et al, (2020), Tian et al. (2020), and Ye et al. (2020). Gray field in panel b represents the full range in δ^{56}Fe observed in the Adagdak samples.

ADG-82-18 yield an average $\delta D = –21 \pm 6$ ‰. Both grains contain less than 0.1 wt% Cl + F.

Oxides: The ultramafic cumulates contain aluminous spinel (Cr# = 33–47) with $\delta^{56}Fe$ ranging from + 0.10 to +0.28 ‰ (Fig. 4d-f). For four cumulate samples, we performed single-grain Fe isotope analysis on two separate spinel grains from each sample (i.e., a total of 8 analyses from 4 samples). The measured values of $\delta^{56}Fe$ for spinel grains from the same sample were consistently within error of each other. For the samples in which we measured the composition of both spinel and coexisting olivine ($n = 5$), $\delta^{56}Fe$ in spinel is positively correlated with $\delta^{56}Fe$ in olivine (Fig. 4c). In the cumulate samples, spinel $\delta^{56}Fe$ shows a weak negative correlation with $Fe^{3+}/\Sigma Fe$ ($r^2 = 0.55$, Fig. 4d) and Cr# ($r^2 = 0.45$, Fig. 4e) and a stronger positive correlation with Mg# ($r^2 = 0.73$, Fig. 4f). Spinel in the mantle dunite is more chromium-rich (Cr#=60) than in the cumulates. The two spinel grains analyzed from the mantle dunite have $\delta^{56}Fe$ of + 0.18 ± 0.04 ‰ and + 0.11 ± 0.02 ‰. Magnetite is the dominant oxide phase in the amphibole gabbro and hornblendite cumulates. The $\delta^{56}Fe$ of three bulk magnetite mineral separates ranges from + 0.11 to +0.13 ‰ (Fig. 5a).

4.2. Lavas

Iron isotope compositions were obtained for five Adagdak lavas, ranging from basalt to andesite. The measured $\delta^{56}Fe$ of the lavas ranges from + 0.03 to +0.06 ‰ (Fig. 5a and Fig. 6a). These values are typical of $\delta^{56}Fe$ observed in arc lavas (Fig. 1) and are similar to previous analyses of Central Aleutian arc lavas reported by Foden et al. (2018) ($\delta^{56}Fe$ = 0.00 to +0.08 ‰; Fig. 6a). While our lava samples do not extend to the high silica concentrations reported for Adagdak dacites by Romick et al. (1992), they span much of the compositional range observed by previous studies (Coats, 1952; Myers et al., 1985; Debari et al., 1987; Kay and Kay, 1985, 1994) of Adagdak basalt and andesite (Fig. 6b). Our samples also do not extend to the high MgO concentrations observed in sample ADAG-81DR (11.83 wt% MgO; Debari et al., 1986), the olivine-phyric host basalt of the Adagdak cumulate suite.

5. Discussion

5.1. *Effects of dehydrogenation on $Fe^{3+}/\Sigma Fe$ in amphibole*

Two lines of evidence suggest that cumulate amphibole experienced dehydrogenation after crystallizing: 1) the presence of an oxo-component (O^{2-}) in amphibole gabbro ADG-CB-1 grain 6 (0.21–0.47 wt%) and hornblendite ADG-82-18 grain 10 (0.49–0.71 wt%; dependent on the uncertainties of water concentrations), and 2) δD values (–16 to –52 ‰ for all measured grains) that are heavier than the average reported measurements for arc magmatic waters as determined from melt inclusions (–60 to –80 ‰; compilation in Ratschbacher et al., 2023) (e. g., Demény et al. (2006)). Dehydrogenation is accompanied by oxidation of ferrous to ferric Fe in the amphibole structure through the following reaction: $Fe^{2+} + OH^- \rightleftharpoons Fe^{3+} + O^{2-} + H^+$. Thus, the $Fe^{3+}/\Sigma Fe$ ratios determined by SMS of amphibole that has experienced dehydrogenation likely do not reflect primary magmatic values. In an effort to estimate the magmatic $Fe^{3+}/\Sigma Fe$ ratios of amphibole during crystallization, we constructed two Rayleigh fractionation inverse models, assuming an initial amphibole $\delta D = –80$ ‰ and H_2O content of 2 wt% (calculations and further details given in the Supplemental Data). These calculations suggest that the $Fe^{3+}/\Sigma Fe$ ratio of ADG-CB-1 grain 6 and ADG-82-18 grain 10 during crystallization were 0.41 ± 0.04 and 0.30 ± 0.05, respectively. Due to its structural complexity, previous studies have not attempted to rigorously constrain the amphibole force constant. Li et al. (2020) estimated an amphibole force constant of 250 N/m based on the relationship between mineral coordination number and $Fe^{3+}/\Sigma Fe$, as discussed by Sossi and O'Neill (2017), and assuming an amphibole $Fe^{3+}/\Sigma Fe$ ratio of 0.53. Using the same method and a representative amphibole gabbro $Fe^{3+}/\Sigma Fe$ ratio 0.41 ± 0.04, we
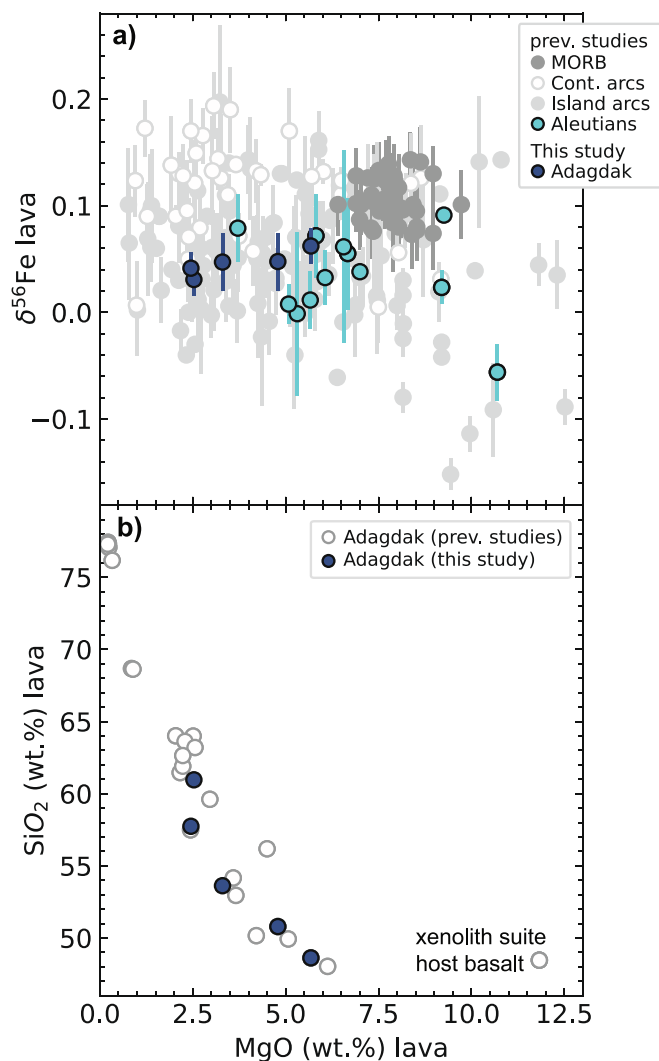

Fig. 6. (a) $\delta^{56}Fe$ of Adagdak lavas vs. MgO (wt.%). The Fe isotope composition of lavas from other island arcs (Dauphas et al., 2009; Williams et al., 2018; Foden et al., 2018; Cooper and Inglis, 2022; Chen et al., 2023; Johnson et al., 2023), continental arcs (Foden et al., 2018; Du et al., 2022), MORBs (Teng et al., 2013), and other Aleutian lavas (Foden et al., 2018) is given for comparison. (b) MgO vs SiO_2, (wt.%) for Adagdak lavas measured in this study compared to literature data (Coats, 1952; Kay and Kay, 1985, 1994; Myers et al., 1985; Romick et al., 1992; Hanna et al., 2020).

estimate an amphibole force constant of 241 ± 9 N/m for an average Adagdak amphibole composition.

5.2. *Preservation of magmatic mineral compositions*

Iron-magnesium ratios in cumulate minerals are susceptible to diffusive exchange between coexisting phases during cooling and lower-crustal residence. Subsolidus equilibration in mafic and ultramafic rocks can result in underestimates of magmatic temperatures when olivine-spinel geothermometry is applied to these assemblages (e.g., Fabriès, 1979; Lehmann, 1983). Studies have shown that subsolidus exchange also affects the Fe and Mg isotope systematics of coexisting phases in igneous rocks, and that spinel group minerals are particularly susceptible to alteration through these processes (e.g., Chen et al., 2014; Bai et al., 2021). To assess whether major element systematics are recording magmatic conditions, we first compare calculated mineral-equilibria temperatures and Fe/Mg ratios of coexisting phases in the Adagdak xenoliths to high-temperature experimental data.

Experiments conducted at conditions relevant to the crystallization of basaltic magmas in the lower oceanic crust (i.e., 0.7–1 GPa, >3 wt% H_2O, fO_2 > FMQ: Blatter et al., 2013; Nandedkar et al., 2014; Ulmer et al., 2018; Marxer et al., 2022) produce dunite, wehrlite, and (±olivine) clinopyroxenite assemblages between 1230 and 1020 °C and an amphibole gabbro assemblage between 1030 and 700 °C (Fig. 7). Apart from clinopyroxenite ADG-82-15, which preserves an anomalously low temperature of 914 + 42/−49 °C, the temperatures calculated with Fe-Mg exchange thermometry for the ultramafic cumulates (1000–1170 °C: Sosa et al., 2023) are consistent with experimental studies. Comparison to experimental data suggests that the temperatures calculated from olivine-spinel thermometry of the olivine clinopyroxenite cumulates (1030 ± 20 °C) are more appropriate estimates for Adagdak clinopyroxenite samples ADG-82-1 and ADG-82-15. Temperature estimates for Adagdak amphibole gabbro cumulates calculated

with amphibole-only thermobarometry (920–970 °C) are also consistent with experimental data, while those obtained through amphibole-plagioclase thermometry (1075–920 °C) are slightly higher but generally in agreement with the range over which experimental studies have crystallized these assemblages.

Co-crystallizing olivine and clinopyroxene from experimental studies of lavas ranging from basalts to Mg-andesites preserve $K_D(Fe^T/Mg)^{cpx-ol}$ (i.e., molar $[Fe^T/Mg]_{ol}/[Fe^T/Mg]_{cpx}$) between 0.7 and 1.6 (Fig. 7; Holloway and Burnham, 1972; Sisson and Grove, 1993; Müntener et al., 2001; Pichavant and Macdonald, 2007; Krawczynski et al., 2012; Blatter et al., 2013; Stamper et al., 2014; Ulmer et al., 2018), consistent with the range observed in coexisting olivine and clinopyroxene in the Adagdak xenoliths ($K_D(Fe^T/Mg)^{cpx-ol}$ = 0.7–1.3). We note that while most (89 %) of the ultramafic Adagdak xenoliths preserve $K_D(Fe^T/Mg)^{cpx-ol}$ between 0.7 and 0.9, samples ADG-8 and ADG-82-1 are outliers with higher K_{DS}

Fig. 7. Comparison of Adagdak data to experimental studies. **A)** Temperature range over which experimental studies crystallized dunite, wehrlite, (±olivine) clinopyroxenite, and amphibole gabbro assemblages compared to calculated crystallization temperatures for cumulate xenoliths. **B)** Fe/Mg ratios in clinopyroxene and olivine from experimental studies compared to those from coexisting clinopyroxene and olivine in the Adagdak xenoliths. **C)** Fe/Mg ratios in clinopyroxene and orthopyroxene from experimental studies compared to those preserved in Adagdak lherzolite ADG-CB-9. Experimental data are from Holloway and Burnham (1972), Sisson and Grove (1993), Gaetani et al. (1998), Müntener et al. (2001), Wasylenki et al. (2003), Pichavant and Macdonald (2007), Krawczynski et al. (2012) Blatter et al. (2013), Green et al. (2014), Stamper et al. (2014), Mandler and Grove (2016), and Ulmer et al. (2018).

of 1.2 and 1.3, respectively. While still within the range observed in experimental studies, this deviation in Fe-Mg partitioning from what is observed in other samples within the suite may indicate that these samples have been affected by subsolidus processes to such an extent that they no longer reflect magmatic conditions. Concerning the Adagdak mantle dunite, orthopyroxene-clinopyroxene pairs in partial melting experiments of mantle peridotites yield $K_D(Fe^T/Mg)^{cpx-opx}$ between 0.8 and 1.4 (Gaetani and Grove, 1998; Wasylenki et al., 2003; Green et al., 2014; Mandler and Grove, 2016), consistent with the value of $K_D(Fe^T/Mg)^{cpx-opx} = 0.8 \pm 0.1$ preserved by sample ADG-CB-9 (Fig. 7).

Taken together, comparisons to experimental studies suggest that—apart from the specific samples discussed above (ADG-8 and ADG-82-15)—the Adagdak cumulates appear to preserve magmatic conditions and appropriate temperature estimates for modeling purposes. Iron-magnesium partitioning between olivine-clinopyroxene and orthopyroxene-clinopyroxene pairs in Adagdak lherzolite ADG-CB-9 also appears to reflect upper-mantle equilibrium conditions.

5.3. Inter-mineral fractionation

We compare measured inter-mineral isotope fractionation factors between co-crystallizing phases in the Adagdak xenoliths to theoretical predictions based on the force constant for Fe in different phases ($\langle F \rangle_{mineral}$) and estimates of crystallization temperature (Sosa et al., 2023). The force constants of olivine, spinel, and magnetite have been measured by previous studies (Polyakov et al., 2007; Dauphas et al., 2012, 2014; Roskosz et al., 2015; Sossi and O'Neill, 2017). Due to their complex crystallographic structures and ability to structurally incorporate both ferric and ferrous Fe, the force constants for clinopyroxene and amphibole have not been determined but can be estimated based on observed inter-mineral fractionation within the cumulates and data from previous studies. The force constants used in these calculations are given in Table 2 and discussed in greater detail in the Supplemental Data.

Within the ultramafic cumulates, spinel is consistently the isotopically heaviest phase ($\delta^{56}Fe = +0.10$ to $+0.28$ ‰), followed by clinopyroxene ($\delta^{56}Fe = -0.05$ to $+0.11$ ‰), and olivine ($\delta^{56}Fe = -0.10$ to $+0.06$ ‰) (Fig. 5). Coexisting clinopyroxene and olivine preserve fractionations of $\Delta^{56}Fe_{cpx-ol} = +0.05$ to $+0.10$ ‰ (Fig. 4b). Similar degrees of clinopyroxene-olivine fractionation are observed in spinel lherzolite xenoliths from the Mexican Basin and Range province ($\Delta^{56}Fe_{cpx-ol} = +0.03$ to $+0.06$ ‰; Williams et al., 2005) and un-metasomatized Mg-lherzolites from the North China Craton ($\Delta^{56}Fe_{cpx-ol} = +0.04$ to $+0.09$ ‰; Zhao et al., 2015). The strong positive correlations between $\delta^{56}Fe$ in coexisting olivine and clinopyroxene in the Adagdak samples ($R^2 = 0.76$), and the similarity between our measured $\Delta^{56}Fe_{cpx-ol}$ for the cumulates and that from previous studies of equilibrated mantle rocks suggest, that the Adagdak cumulates also record isotopic equilibrium

Table 2
Force constants used in modeling.

Phase	$\langle F \rangle$ (N/m)	Source
Olivine (Fo$_{82}$)	197 ± 10	NRIXS, Dauphas et al. (2014)
Clinopyroxene	239 ± 13	Estimate from observed olivine-cpx fractionation
Orthopyroxene (En$_{93}$)	195 ± 5	NRIXS, Jackson et al. (2009)
Spinel: Fe^{+2} in MgFeAl	190 ± 15	NRIXS, Roskosz et al. (2015)
Spinel: Fe^{+3} in MgFeAl	302 ± 18	NRIXS, Roskosz et al. (2015)
Amphibole	241 ± 9	Estimate from synchrotron Mössbauer spectroscopy
Magnetite	264 ± 6	NRIXS, Roskosz et al. (2015)
Fe^{2+} in basalt	193 ± 7	NRIXS, Roskosz et al. (2022)
Fe^{3+} in basalt	364 ± 23	NRIXS, Roskosz et al. (2022)

between co-crystallizing clinopyroxene and olivine. Using the observed clinopyroxene-olivine fractionation, temperature constraints from Fe-Mg exchange thermometry (Sosa et al., 2023) comparisons to experimental studies, and the known relationship between inter-mineral fractionation factors and force constants ($\Delta_{B-A} = (\delta_B - \delta_A) = 2853[\langle F \rangle_B - \langle F \rangle_A]/T^2$; Dauphas et al., 2014), we can estimate an appropriate clinopyroxene force constant from our data. Using the range of observed values for $\Delta^{56}Fe_{cpx-ol}$ (0.05–0.10 ‰), an average crystallization temperature of 1060 °C for the ultramafic assemblages, and an olivine force constant of 197 ± 10 N/m (Dauphas et al., 2014), our data suggest the clinopyroxene force constant should be between 227 and 262 N/m. Taking the average observed clinopyroxene-olivine fractionation of $\Delta^{56}Fe_{cpx-ol} = 0.07 \pm 0.02$ ‰, we use an estimate of $\langle F \rangle_{cpx} \approx 239 \pm 13$ N/m in our modeling moving forward.

Force constants for Adagdak spinel were calculated using the parameterization of Roskosz et al. (2015), where $\langle F \rangle = 190 \pm 15$ N/m for Fe^{2+} in Mg-Fe-Al spinel and $\langle F \rangle = 302 \pm 18$ N/m for Fe^{3+}. Spinel $Fe^{3+}/\Sigma Fe$ ratios were taken from Sosa et al. (2023), who calculated Fe speciation following the methods of Wood and Virgo (1989). For these analyses, spinel is analyzed in a separate EPMA session, and every 150–200 spinel analyses are bracketed by measurements of spinel grains whose $Fe^{3+}/\Sigma Fe$ ratios have previously been determined through Mössbauer spectroscopy (Wood and Virgo, 1989; Bryndzia and Wood, 1990). Spinel $Fe^{3+}/\Sigma Fe$ ratios for unknown samples, which are initially calculated from EPMA data through charge balance, are then adjusted using the correction scheme of Wood and Virgo (1989) (see Davis et al., 2017 for a recent discussion of the method). Calculated $Fe^{3+}/\Sigma Fe$ ratios for the measured Adagdak cumulate spinel range from 0.39 to 0.41 (Supplemental Data, Table S6), and using the parameterization of Roskosz et al. (2015), yield spinel force constants between 233 and 236 N/m.

The fractionation factor between coexisting Adagdak spinel and olivine ranges from $\Delta^{56}Fe_{spl-ol} = +0.12$ to $+0.28$ ‰. Dunite, wehrlite, and olivine clinopyroxenite cumulates from Adagdak preserve equilibrium temperatures between 1000 and 1170 °C (Sosa et al., 2023). Using the average spinel force constant of 235 N/m and an olivine force constant of 197 (Dauphas et al., 2014), calculated estimates for equilibrium spinel-olivine fraction over this temperature interval are considerably lower, ranging from $\Delta^{56}Fe_{spl-ol} = +0.05$ to $+0.07$ ‰. High degrees of spinel-olivine fractionation have also been previously observed in mantle lherzolite xenoliths ($\Delta^{56}Fe_{spin-ol}$ of $+0.2$ to $+0.4$ ‰; Zhao et al., 2015; Williams et al., 2015) (Fig. 8). These large inter-mineral fractionations between spinel and other mantle minerals have been attributed to disequilibrium developed during metasomatism or partial melting (Williams et al., 2005; Zhao et al., 2015; Roskosz et al., 2015). Additionally, measured spinel-clinopyroxene fractionations in the Adagdak cumulates range from $\Delta^{56}Fe_{spl-cpx} = +0.06$ to $+0.19$ ‰. Using our estimated clinopyroxene force constant of 239 N/m and an average spinel force constant of 235 N/m, the equilibrium fractionation between coexisting Adagdak spinel and clinopyroxene should be $\Delta^{56}Fe_{spl-cpx} \approx 0.0$ ‰ at 1050 °C.

The large inter-mineral isotopic fractionation between spinel and other phases suggests that spinel Fe isotope ratios do not record equilibrium conditions during crystallization in the cumulates. Instead, their Fe isotopic composition may reflect subsequent (partial) re-equilibration via Fe-Mg diffusion during their residence in the lower crust. Subsolidus exchange of Mg and Fe^{2+} between spinel and olivine during cooling has been well documented in experimental studies (e.g., Ozawa, 1984; Liermann and Ganguly, 2002; Vogt et al., 2015), resulting in a loss of Fe from spinel to olivine. Small spinel grains, such as those in the Adagdak cumulates (10–300 μm in diameter), are particularly susceptible to Fe loss during cooling (Ozawa, 1984), and their Fe isotope composition would be more affected by this process as compared to modally dominant olivine. The greatest spinel-olivine fractionation is also observed in the most olivine-rich cumulates (dunite: $\Delta^{56}Fe_{spin-ol} = +0.20$ to $+0.28$ ‰, wehrlite: $\Delta^{56}Fe_{spin-ol} = +0.12$ to $+0.24$ ‰). Spinel

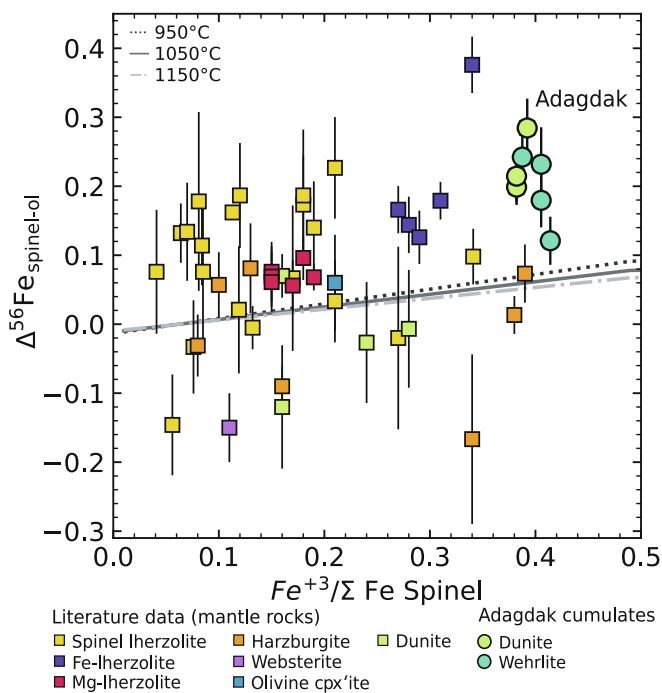**Fig. 8.** $\Delta^{56}Fe_{spinel-olivine}$ (‰) for Adagdak cumulates and mantle rock. Gray lines represent equilibrium fractionation at a given spinel $Fe^{3+}/\Sigma Fe$ (Roskosz et al., 2015) at 950 to 1150 °C, with an olivine force constant of 197 N/m. Literature data are from Macris et al. (2015), Williams et al. (2005), Xiao et al. (2016), Zhao et al., (2010,2015).

from all Adagdak cumulates shows core-to-rim increases in Mg# (+0.2 to +1.4), consistent with the idea that the rims of these small grains were affected by subsolidus Fe-Mg diffusion with neighboring olivine. If the effects of post-cumulus Fe-Mg exchange were concentrated in grain rims, this may partially explain why temperatures obtained through Fe-Mg exchange thermometry appear to be recording magmatic conditions, as these temperatures were calculated exclusively with core compositions.

Using temperature estimates and the known force constant of spinel and olivine, we can estimate theoretical $\delta^{56}Fe$ values of cumulate spinel. Crystallization experiments on primitive basalts conducted under conditions relevant to the lower arc crust (0.7–1 GPa, 3–4 wt% initial H_2O, fO_2 = NNO to NNO + 2) typically crystallize dunite and wehrlite assemblages between the liquidus (~1200 °C) and ~ 1050 °C (Blatter et al., 2013; Nandedkar et al., 2014; Ulmer et al., 2018). Between 1200 and 1050 °C, the calculated equilibrium fractionation between spinel with $Fe^{3+}/\Sigma Fe$ = +0.38 to +0.41 (the range observed in spinel from Adagdak cumulates) and olivine is $\Delta^{56}Fe_{spl-ol}$ = +0.05 to +0.07 ‰. This would imply that olivine in the Adagdak dunite and wehrlite cumulates ($\delta^{56}Fe$ = –0.08 to +0.06 ‰) would have been in equilibrium with spinel with $\delta^{56}Fe$ between –0.03 and +0.13 ‰ during crystallization. Even considering the errors on reported spinel and olivine force constants, the maximum force constants for the Adagdak spinel would be 250–257 N/m. Using a minimum olivine force constant of 187 N/m, this would yield $\Delta^{56}Fe_{spl-ol}$ = 0.07 to 0.10 ‰ and imply that olivine in the Adagdak dunite and wehrlite cumulates would have crystallized in equilibrium with spinel with $\delta^{56}Fe$ –0.01 to +0.16 ‰, values which are still below the observed range some cumulate spinel ($\delta^{56}Fe$ = +0.10 to +0.28 ‰).

In the amphibole gabbro and hornblendite xenoliths, magnetite is consistently the phase with the highest $\delta^{56}Fe$ (+0.10 to +0.13 ‰), followed by amphibole (+0.07 to +0.09 ‰) and clinopyroxene (+0.05 to +0.07 ‰). Although we only have measurements of coexisting clinopyroxene and amphibole from two cumulates (amphibole gabbro samples ADG-6 and ADG-CB-1), these samples show similar degrees of

amphibole-clinopyroxene fractionation with $\Delta^{56}Fe_{amph-cpx}$ = –0.01 to +0.01 ‰. While Fe isotope measurements of coexisting amphibole and clinopyroxene are scarce in the literature, similarly small degrees of amphibole-clinopyroxene fractionation have also been observed in mineral separates from augite syenites in the Ilímaussaq Complex by Schoenberg et al. (2009) ($\Delta^{56}Fe_{amph-cpx}$ = +0.03 ± 0.05 ‰), who interpreted these samples as preserving near isotopic equilibrium.

As our estimated force constants of amphibole and clinopyroxene (241 and 239 N/m, respectively) are within error of each other, we predict $\Delta^{56}Fe_{amph-cpx} \approx$ 0.0 ‰ at equilibrium assuming an average crystallization temperature of 970 °C for the amphibole gabbro cumulates. In conjunction with comparisons to literature data and considering the typical errors of these measurements (0.02–0.03 ‰), this suggests that amphibole-clinopyroxene pairs are recording isotopic equilibrium within the amphibole gabbro cumulates. While we only have measurements of co-crystallizing clinopyroxene and magnetite from one cumulate (ADG-74) and no measurements of coexisting amphibole and magnetite, the average Fe isotope compositions of these phases in the amphibole gabbro cumulates preserve magnetite-silicate fractionations of $\Delta^{56}Fe_{mag-cpx}$ and $\Delta^{56}Fe_{mag-amph} \approx$ +0.05 ‰. Using a magnetite force constant of 264 N/m (Roskosz et al., 2015) and our estimated force constants for clinopyroxene and amphibole, we calculate equilibrium fractionations of $\Delta^{56}Fe_{mag-cpx}$ and $\Delta^{56}Fe_{mag-amph}$ = +0.05 ‰ at 970 °C, consistent with our measurements. Coexisting magnetite and amphibole phenocrysts in basaltic andesites and dacites from Mount Lassen, California, show similar degrees of magnetite-amphibole fractionation ($\Delta^{56}Fe_{mag-amph}$ = –0.02 ± 0.09 ‰; Beard and Johnson, 2004). In summary, the observed inter-mineral fractionation suggests that—within the amphibole gabbro samples—amphibole, magnetite, and clinopyroxene are recording equilibrium conditions. Within the ultramafic cumulates, olivine and clinopyroxene appear to be recording crystallization conditions, while spinel does not, likely due to subsolidus Fe-Mg exchange.

5.4. Isotopic evolution of Adagdak cumulates

Combining our Fe isotope measurements of cumulate mineral separates and whole-rock powders, we can evaluate the extent to which fractionation of different phases drives the isotopic evolution of the cumulate suite and, by extension, their parental melts during differentiation. Within the ultramafic cumulates, our data suggest that whole-rock Fe isotope compositions are strongly dependent on the modal proportion of olivine and clinopyroxene. Because clinopyroxene is consistently 0.05–0.10 ‰ heavier than coexisting olivine, the increase in bulk $\delta^{56}Fe$ observed between the most primitive dunite xenoliths ($\delta^{56}Fe$ = –0.09 to –0.02 ‰) and more evolved (±olivine) clinopyroxenite samples ($\delta^{56}Fe$ = +0.06 to +0.09 ‰) reflects the increasing modal proportion of clinopyroxene relative to olivine. This transition from dunite to clinopyroxenite corresponds to an increase up to 0.18 ‰ in whole-rock $\delta^{56}Fe$ for the cumulates. Although spinel is the most Fe-rich phase in the ultramafic cumulates (21.0–33.7 wt% FeO_T), its low modal abundance (0–7 % modally for all samples, ≤1 % by volume for 60 % of cumulates) means that spinel never contains more than ~30 % of the whole-rock FeO_T budget in the ultramafic cumulates (Fig. 9). By contrast, olivine contains 59–93 % of bulk FeO_T in the Adagdak dunite and wehrlite cumulates while clinopyroxene contains 30–90 % of the bulk FeO_T in the (±olivine) clinopyroxenite cumulates (Fig. 9).

Within the amphibole and magnetite-bearing samples, there is no correlation between MgO and whole-rock $\delta^{56}Fe$ (Fig. 4a). The elevated and relatively uniform $\delta^{56}Fe$ of these samples ($\delta^{56}Fe$ = +0.04 to +0.08 ‰) reflects their high modal proportions of isotopically heavy magnetite ($\delta^{56}Fe$ = +0.11 to +0.13 ‰) and amphibole ($\delta^{56}Fe$ = +0.06 to +0.09 ‰). Although amphibole is not as isotopically heavy as coexisting magnetite and contains lower Fe concentrations (9.9——12.6 wt% FeO_T for amphibole vs. 79–81 wt% FeO_T for magnetite), the high modal abundance of amphibole in the Adagdak amphibole gabbro and
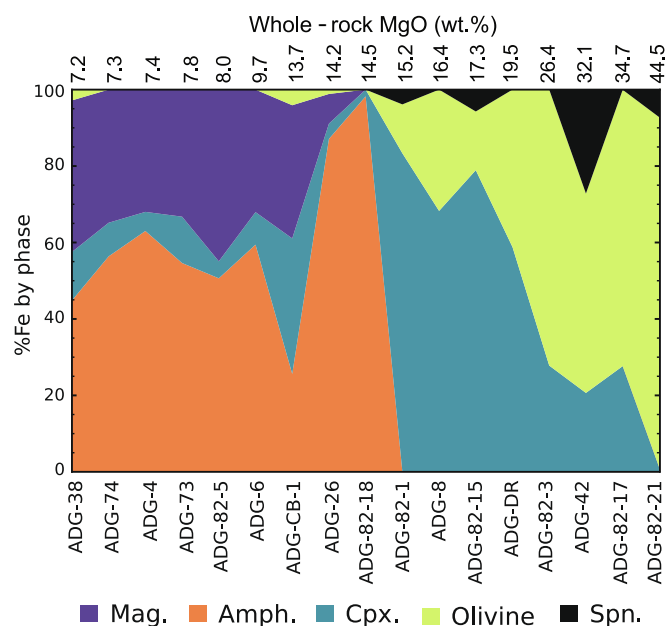
Fig. 9. Percent of bulk whole-rock FeO$_T$ budget held by each phase in Adagdak cumulates, calculated from modal abundances and mineral chemistry. Samples are organized by increasing MgO.

hornblendite cumulates (30–97 % by volume) means that amphibole contains between 28 and 99 % of the FeO$_T$ budget for these samples (Fig. 9). We therefore argue that, in addition to magnetite, amphibole fractionation should exert a strong effect on the isotopic evolution of these cumulates and their parental liquids.

Cooper and Inglis (2022) also argued that amphibole fractionation must play an important role in the Fe isotope evolution of cumulate and non-cumulate gabbro from the Lesser Antilles. The isotopically lightest samples from this suite also had the lowest Dy/Yb ratios, suggesting that they had crystallized from a melt that had been depleted in both Dy and heavy Fe isotopes by amphibole fractionation (Cooper and Inglis, 2022). Although the Adagdak cumulates are not as evolved as those from the Lesser Antilles (Fig. 3), given the isotopically heavy compositions of measured amphibole separates (δ^{56}Fe = +0.07 to +0.09 ‰) and whole-rock hornblendite powders (δ^{56}Fe = +0.07 to +0.08 ‰), it is also reasonable to predict that continued fractionation of amphibole-rich assemblages would deplete more evolved Adagdak melts in heavy isotopes of Fe. Although we cannot directly tie the lava record to the cumulates, correlations in Adagdak lavas between SiO$_2$ and Mg# and indices of amphibole fractionation like La/Yb are consistent with the idea that that amphibole fractionation may have driven the evolving parental melts of the cumulates towards lower δ^{56}Fe (Fig. S8). The implications of amphibole and magnetite fractionation on the evolutions of Adagdak magmas will be discussed further in our analyses of the Fe isotope composition of Adagdak lavas and in modeling.

In summary, the Adagdak cumulate record preserves a complex history of lower- to mid-crustal differentiation and Fe isotope evolution. Lower crustal cumulates first evolved to heavier isotopic compositions as clinopyroxene replaced olivine as the dominant fractionating phase. Once magnetite and amphibole entered the cumulate assemblage, the Fe isotope composition of bulk assemblages remained heavy and relatively constant. Continued fractionation of these isotopically heavy magnetite and amphibole-rich assemblages should have driven late-stage melts towards light Fe isotope ratios, but our samples are not evolved enough to robustly assess this inference analytically.

5.5. Mantle dunite

Subarc mantle peridotites display a wide range of Fe isotope compositions (δ^{56}Fe = –0.37 to +0.11 ‰), which extend to isotopically lighter values than are observed in mid-ocean ridge (MOR) peridotite (Fig. 1, δ^{56}Fe = –0.09 to +0.11 ‰; Craddock et al., 2013; Sossi et al., 2016). While Adagdak mantle dunite ADG-CB-9 (δ^{56}Fe = –0.03 ± 0.05 ‰) falls within the range observed for MOR peridotites, it is likely isotopically lighter than the MOR peridotite average of + 0.01 ± 0.01 ‰ (Craddock et al., 2013). Depletion in heavy Fe isotopes in arc peridotites may reflect one or a combination of the following processes: (1) incompatible Fe^{3+} behavior during partial melting, with the heavier isotopes of Fe preferentially being extracted from the residue (Williams et al., 2004; Williams and Bizimis, 2014); (2) metasomatism from isotopically light fluids or melts fluxed from the slab (Zhao et al., 2010, 2012; Poitrasson et al., 2013); or (3) disequilibrium isotopic diffusion between melts and mantle wall rock during channelized ascent (Weyer and Ionov; 2007; Teng et al., 2011; Foden et al., 2018; Turner et al., 2018). In this last scenario, because light isotopes of Fe diffuse faster than heavy isotopes, disequilibrium fractionation between percolating melts and mantle olivine results in a net transfer of isotopically light Fe to the peridotite.

Previous studies have shown that partial melts of metamorphosed subducted forearc material or possibly the subducted slab yielded important trace element contributions to the parental magmas of Adak cumulates (Yogodzinski and Kelemen, 2007; Sosa et al., 2023) and other plutonic rocks on Adak Island (Kay et al., 2019). Hence it is possible that the slight isotopic depletion observed in lherzolite ADG-CB-9 stems from melt-rock reactions with partial melts of altered oceanic crust (AOC) or subducted forearc material. The Fe isotope composition of a component derived from the slab itself may be highly variable and would strongly depend on where in the slab the contribution was sourced from and whether it took the form of a melt or fluid. For example, hydrothermal fluids fluxed from the slab are isotopically light, and their progressive removal during subduction should increase δ^{56}Fe in the remaining AOC (Rouxel et al., 2003, 2008). Partial melting of this enriched source would be expected to produce isotopically heavy melts, particularly if garnet remained in the residue, which would retain the light isotopes of Fe (He et al., 2017; Sossi and O'Neill, 2017). However, reduced fluids leached from the slab may also precipitate veins of isotopically light secondary sulfides and Fe oxyhydroxides (δ^{56}Fe as low as –0.71 ‰ Rouxel et al., 2003) within the slab, creating regions with highly depleted Fe isotope compositions. It is however unlikely that sediment subduction significantly affected the Fe isotope composition of the mantle wedge beneath Adagdak, as previous studies have shown subducted sediments to be isotopically heavy (δ^{56}Fe = +0.05 to +0.18 ‰, Nebel et al., 2015). The radiogenic isotope systematics of arc lavas globally are also consistent with a small net transfer of subducted sediment to the subarc mantle (<4 %, Hawkesworth et al., 1993), particularly for the Central Aleutians (0.2–0.6 % by mass sediment transfer, Nielsen et al., 2016).

Regardless of whether the mantle dunite analyzed here experienced an isotopic depletion or metasomatic event, the sample provides our best constraints on the Fe isotope systematics of the subarc mantle beneath Adagdak. Using the mantle melting equations of Dauphas et al. (2009), the calculated Fe isotope composition of magmas generated by 10 % buffered fractional melting at fO$_2$ = FMQ + 1 of our mantle dunite (δ^{56}Fe = –0.03 ± 0.05 ‰) ranges from δ^{56}Fe = –0.08 to +0.02 ‰ (see Supplemental Data for a full discussion of modeling). This is consistent with the previous study of Aleutian magmas by Foden et al. (2018), who report a δ^{56}Fe value of 0.00 to +0.08 ‰ for Central Aleutian lavas.

5.6. Implications for Adagdak melts

While we cannot establish a direct petrogenic relationship between the cumulate xenoliths and Adagdak lavas, we can use comparisons to

experimental studies to evaluate whether the lavas may represent a complement to the xenoliths over a given interval of differentiation. Cumulate assemblages with similar mineral chemistry, modal proportions, and bulk compositions to the Adagdak cumulate suite have been produced in experiments that fractionally crystallize primitive hydrous basalts (H2Oinitial = 3–3.6 wt%, Mg# = 67–76) at conditions relevant to the lower arc crust (1–0.7 GPa, fO2 = NNO-NNO + 2; Nandedkar et al., 2014; Ulmer et al., 2018). These experiments produced melt compositions similar to our most primitive measured Adagdak basalt (ADAG-81–4: 48.6 wt% SiO2, Mg# = 49.6, Kay and Kay, 1994) after 40–55 % crystallization of olivine, clinopyroxene, and spinel, just before amphibole and magnetite saturated as cumulate phases (Nandedkar et al., 2014; Ulmer et al., 2018). This suggests that the Adagdak basalts and andesites measured here are capturing a complementary record of melt evolution to our more evolved cumulate compositions (namely, the amphibole gabbro and hornblendite cumulates).

In contrast to the cumulate data, which show pronounced evolutionary trends, Fe isotope compositions of the Adagdak lavas are all within error of each other (δ^{56}Fe = +0.03 ± 0.02 to +0.06 ± 0.02: Fig. 6a). While there are suggestions of slight positive correlations between average δ^{56}Fe and indices of differentiation like MgO (Fig. 6a), the resolution on the data are not suitable to assess whether the melts are in fact becoming isotopically lighter with decreasing MgO. These data reveal fundamental issues with studying the Fe isotope systematics of lavas in isolation. Mass balance dictates that δ^{56}Fe of the parental lavas should change gradually over restricted melt fractions if the majority of Fe in the system remains in the melt during crystallization. As our samples do not fully encompass the compositional diversity of all Adagdak lavas (Fig. 6b), it is perhaps not surprising that over this restricted range in melt composition (48.6–61 wt% SiO2, 5.7–2.5 wt% MgO), the Fe isotope composition of the melt varies almost negligibly. The isotopic fractionation associated with crystallization and magmatic evolution may, therefore, be more apparent in the cumulate record than in their complementary lavas. The highly magnesian nature of the Adagdak dunite and wehrlite cumulates also suggests that these samples crystallized from a primitive basalt (Mg# = ~66–76) as compared to the more evolved lava compositions analyzed here (Debari et al., 1986; Sosa et al., 2023). Our data also show that most primitive cumulates were isotopically light (δ^{56}Fe = –0.02 to +0.09 ‰), and fractionation of these assemblages should serve to increase the δ^{56}Fe of the remaining melt. This implies that there was likely a period of enrichment in heavy Fe isotopes during early crystallization of Adagdak basalts that the lava record fails to capture.

5.7. Modeling the isotopic evolution of the melts parental to the Adagdak cumulates

To illustrate the effect that fractional crystallization can have on the Fe isotope systematics of arc magmas, we use our Adagdak data to construct a mass balance fractionation model, in which our bulk cumulate compositions are removed from a basaltic melt with an initial composition of δ^{56}Fe = 0.0 ‰. Note that changing δ^{56}Fe of the initial melt to any value within our predicted range (δ^{56}Fe = –0.03 to +0.05 ‰) merely serves to shift the isotopic composition of our modeled melts and cumulates to isotopically lighter or heavier values and does not affect the degree of predicted fractionation. The purpose of this model is to illustrate the complex isotopic evolution magmas and their crystallization products may experience as fractionated assemblages change from isotopically light dunite and wehrlite to heavier clinopyroxenite cumulates to isotopically heavy amphibole + magnetite-bearing rocks. Our discussion below focuses on the most salient features of this model and the insights it provides into the isotopic evolution of the Adagdak cumulates and their parental melts. An additional detailed discussion of this modeling approach and the parameters used is given in the Supplemental Data (Figures S12-S14, Tables S13-S15).

Roskosz et al. (2022) showed that the force constant of glasses with

basaltic and andesitic compositions is nearly a linear function of their $Fe^{3+}/\Sigma Fe$ ratio. Although we do not know the $Fe^{3+}/\Sigma Fe$ ratio of the melts parental to the cumulates, we can approximate an appropriate value based on fO2 estimates for the xenoliths themselves (Sosa et al., 2023). Oxygen fugacity estimates for the Adagdak cumulates range from $\Delta FMQ + 0.10$ to +2.14, with an average value of $\Delta FMQ \approx +1$ (Sosa et al., 2023). Using the high-Mg basalt from Ulmer et al. (2018) as a reference basalt, a temperature of 1050 °C, a pressure of 1 GPa, and an fO2 of FMQ + 1, we used the parametrization of Kress and Carmichael (1991) to estimate an appropriate $Fe^{3+}/\Sigma Fe$ ratio for the parental melts to the cumulates, which yielded a value of $Fe^{3+}/\Sigma Fe = 0.22$. The parameterization of Roskosz et al. (2022) then yields an initial force constant of 230 N/m for our basaltic melt.

The major element evolution of the fractionating melt was modeled through stepwise removal of representative bulk cumulate assemblages from a high-Mg basalt (Ulmer et al., 2018) (Table S8). Based on these major element constraints, we constructed an isotope fractionation model in which a primary mantle melt at fO2 = FMQ + 1 with an initial $Fe^{3+}/\Sigma Fe$ of 0.22 fractionates 10 % dunite, 9 % wehrlite, 7 % olivine clinopyroxenite, 3 % clinopyroxenite, and 20 % of an amphibole gabbro assemblage (Fig. 10). Representative whole-rock $Fe^{3+}/\Sigma Fe$ ratios estimated from the model proportions, chemistry, and density of minerals for each lithological group (Table 3). For these calculations, we assumed
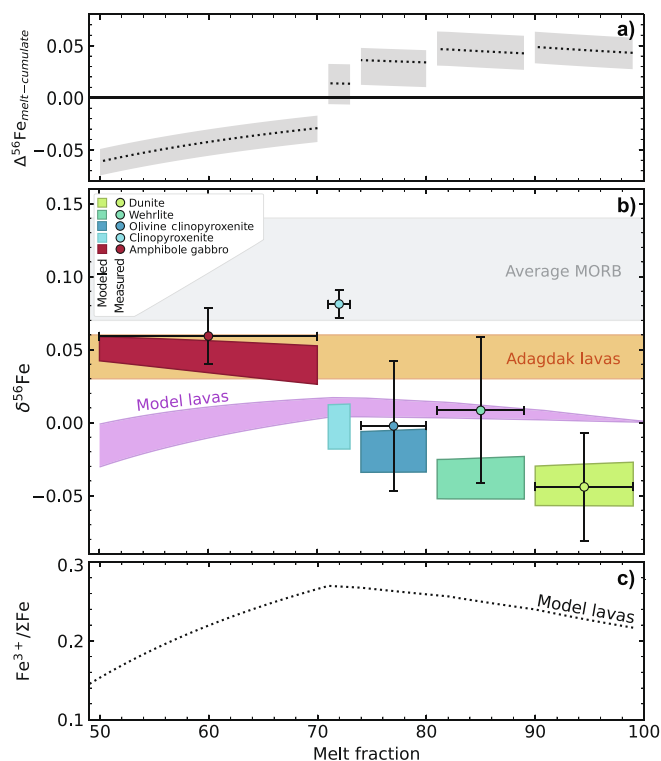

Fig. 10. Mass balance model of Fe isotope evolution of Adagdak melts and cumulates during fractional crystallization. Results are shown as a function of melt fraction. A) Evolution of $\Delta^{56}Fe_{melt-cumulate}$ in model, with errors reflecting uncertainties on reported and estimated melt and mineral force constants B) δ^{56}Fe of modeled melts and cumulates. The weighted average measured cumulate composition for each lithological group is shown as data points with error bars over the interval where that lithology was fractionated in the model. Vertical error bars represent the uncertainty on the composition of the weighted average for each lithological group and horizontal bars represent the range over which each lithology was fractionated from the melt. Colored boxes represent the modeled cumulate compositions. The range in δ^{56}Fe of the modeled cumulates and the melts reflects the uncertainty on reported and estimated melt and mineral force constants. MORB field (gray) is from Teng et al. (2013) and Adagdak lava field represents the range in δ^{56}Fe of measured Adagdak lavas (this study). C) Evolution of $Fe^{3+}/\Sigma Fe$ in modeled melts.

Table 3

Compositions, temperature estimates, and cumulate force constants used in modeling.

Lithology	Dunite	Wehrlite	Olivine clinopyroxenite	Clinopyroxenite	Amphibole gabbro
SiO_2	38.81	45.75	48.45	50.40	42.40
TiO_2	0.10	0.16	0.26	0.37	1.21
Al_2O_3	0.93	2.49	3.16	5.06	18.56
Fe_2O_3	0.49	0.57	0.69	0.85	6.45
FeO	12.09	8.63	5.86	4.23	5.20
MnO	0.00	0.15	0.00	0.09	0.02
MgO	46.08	30.06	23.91	16.49	8.97
CaO	0.97	12.03	17.36	22.19	15.74
Na_2O	0.00	0.13	0.24	0.20	1.30
K_2O	0.01	0.00	0.01	0.02	0.23
$\langle F \rangle$ (N/m)	200 ± 10	206 ± 8	215 ± 3	230 ± 7	256 ± 7
Temp (°C)	1068 ± 33	1037 ± 31	1029 ± 20	1029 ± 20	973 ± 54

olivine contained negligible Fe^{3+}. Clinopyroxene $Fe^{3+}/\Sigma Fe$ ratios were estimated using the normalization scheme of Wood and Banno (1973), and magnetite and spinel $Fe^{3+}/\Sigma Fe$ ratios were calculated from EPMA data based on charge balance. For amphibole, we assumed a uniformed magmatic $Fe^{3+}/\Sigma Fe$ ratio of 0.4 based on our Mössbauer data. Published and estimated Fe force constants for clinopyroxene, olivine, spinel, magnetite, basalt, and amphibole were used to calculate bulk force constants for these cumulates (Table 2). Combined with previously published temperature estimates (Sosa et al., 2023), these bulk force constants were used to calculate cumulate-melt fractionation factors as each lithological group was fractionated from the melt. The representative whole-rock compositions for each lithological group and temperature estimates used in modeling are given in Table 3.

Due to the affinity of olivine for isotopically light Fe relative to basalt, fractionation of olivine-dominated assemblages slightly increases the $\delta^{56}Fe$ in the remaining basalt. Because our estimated clinopyroxene force constant is higher than that of olivine and the same as that of basalt (Table 2), as clinopyroxene replaces olivine as the modally dominant phase at lower melt fractions, cumulate force constants approach that of the melt. The result of this is that during the last interval of ultramafic cumulate crystallization, the degree of cumulate-melt fractionation decreases from $\Delta^{56}Fe_{melt-cumulate} = +0.04$ to $+0.01$ ‰. Once amphibole and magnetite-bearing assemblages begin to crystallize, the force constant of the fractionated cumulates exceeds that of the melt, and $\delta^{56}Fe$ of the melt decreases, as heavier isotopes of Fe are preferentially incorporated into the cumulates ($\Delta^{56}Fe_{melt-cumulate} = -0.03$ to -0.06 ‰). This dichotomy between the fractionation of isotopically light and heavy cumulates is shown in Fig. 10, with the modeled ultramafic cumulates falling below the modeled magma composition at higher melt fractions (>70 %), and the amphibole and magnetite-bearing assemblages falling above the modeled composition at lower melt fractions (50–70 %).

A notable shortcoming of our model is its failure to reproduce the clinopyroxenite assemblages, which showed far higher measured values ($\delta^{56}Fe = 0.06 – 0.09$ ‰) than are predicted by our model ($\delta^{56}Fe = -0.02 – 0.01$ ‰). This discrepancy may come from two potential sources. First, it may be an artifact of applying the same clinopyroxene force constant throughout the entire model. If clinopyroxene in the clinopyroxenite cumulates have higher $Fe^{3+}/\Sigma Fe$ ratios than those in the wehrlite and olivine clinopyroxenite lithologies (which we used to calculate $< F>_{cpx}$ from $\Delta^{56}Fe_{cpx-ol}$), then a higher clinopyroxene force constant should be used. A second possibility is that the clinopyroxenite cumulate pile was infiltrated by a percolating melt at sub-solidus temperature during lower crustal residence. This would be consistent with the anomalously low Fe-Mg exchange thermometry temperature estimates obtained for clinopyroxenite ADG-82-15 (914 + 42/–49 °C) and the presence of small quantities of peritectic amphibole (<1 % by volume) at clinopyroxene grain boundaries noted in samples from this lithological group (Sosa et al., 2023).

5.8. Implications for the Fe isotopic composition of the oceanic arc plutonic record

Our Fe isotope measurements of mineral separates show that different phases in the cumulate sequence have strong and systematic affinities for isotopically heavy versus light Fe. This means that the crystallization sequence and the proportions of specific phases fractionating from the melt exert first-order controls on the isotopic composition of the bulk cumulate removed from the magma, and by extension, the isotopic evolution of parental melts. Fractionation of isotopically light dunite and wehrlite cumulates might produce an interval of increasing $\delta^{56}Fe$ in primitive arc basalts, while the removal of isotopically heavy clinopyroxenite, hornblendite, and amphibole gabbro assemblages results in depletion of heavy Fe isotopes in more evolved basalts and andesites. Our data also imply the existence of (1) a lower crustal layer of low $\delta^{56}Fe$ (<0‰) ultramafic cumulates (dunite and wehrlite) in the Aleutian arc crust and (2) a mid-crustal reservoir of clinopyroxenite, hornblendite, and amphibole gabbro cumulates with higher $\delta^{56}Fe$ (>0.05 ‰).

This is consistent with the previous study of Cooper et al. (2016), who found mid-crustal amphibole + plagioclase-bearing cumulates from Statia, Lesser Antilles ($\delta^{56}Fe = +0.09$ to $+0.12$ ‰), to be isotopically heavier than their complementary non-cumulate gabbros and lavas ($\delta^{56}Fe = +0.01$ to $+0.06$ ‰), suggesting that fractionation of these isotopically heavy assemblages depleted later stage melts in heavy Fe isotopes. Li et al. (2020) also argue that mid-crustal amphibole fractionation played an important role in the isotopic evolution of intrusive rocks from the Tongde region, South China, depleting the more evolved diorite compositions in the heavy isotopes of Fe. If the plutonic non-cumulate rocks on Adak Island (namely the calc-alkaline Hidden Bay pluton, Kay et al., 1990, 2019) are an upper crustal complement to the mid-crustal cumulates (Sosa et al., 2023), and represent crystallized melts that have experienced prolonged Fe isotope depletion from magnetite and amphibole fractionation, then we might also suspect these rocks to be isotopically light relative to the amphibole gabbro and hornblendite cumulates. Furthermore, our results suggest that for oxidized hydrous arc systems, amphibole—independent of magnetite—may play a role in generating the depletion in heavy Fe isotopes observed in erupted lavas (consistent with the conclusions of Li et al., 2020, and Cooper and Inglis, 2022).

Our results also support previous studies that have suggested that amphibole may play a key role in driving Fe-depletion trends in calc-alkaline magmas (Kay et al., 1991; Romick et al., 1992; Kay and Mpodozis, 2001; Walters et al., 2020; Barber et al., 2021; Du et al., 2022), with the greatest proportion of the bulk Fe content for the hornblendite and amphibole gabbro cumulates typically (90 % of studied cumulates) hosted in amphibole (28–99 % of the FeO_T budget) rather than in magnetite (0–46 % of the FeO_T budget) (Fig. 9). However, with regards to Fe isotopes, the role of amphibole in dictating the trajectory of

isotopic evolution might be complicated by the fact that studies have shown amphibole $Fe^{3+}/\Sigma Fe$ ratios to be highly variable in arc systems ($Fe^{3+}/\Sigma Fe$ = 0.14–0.64, Ratschbacher et al., 2023). Previous studies have shown that oxidation state and Fe coordination number are equally important in governing the ability of phases to accept heavy versus light isotopes of Fe, with minerals having higher $Fe^{3+}/\Sigma Fe$ ratios and lower Fe coordination numbers preferring the heavier isotopes (Roskosz et al., 2015; Sossi and O'Neill, 2017; Nie et al., 2021). While garnet fractionation (which has been suggested to be important in continental arcs with thicker crusts) should drive the remaining melt to higher $\delta^{56}Fe$, and magnetite fractionation to lighter Fe isotope compositions, amphibole fractionation may have the potential to drive arc melts Fe isotope compositions to lighter of heavier $\delta^{56}Fe$ values depending on fO_2 and amphibole $Fe^{3+}/\Sigma Fe$. Clinopyroxene might also play a dual role in governing the Fe isotope trajectories of arc melts, as Mössbauer studies of mantle peridotites have shown variable clinopyroxene $Fe^{3+}/\Sigma Fe$ ratios ($Fe^{3+}/\Sigma Fe$ = 0.05–0.37; Dyar et al., 1992; Luth and Canil, 1993; Woodland, 2009; Hao and Li, 2013). Given that amphibole and clinopyroxene are both modally abundant phases in arc-related cumulates, our understanding of the Fe isotope systematics of arc magmas would benefit greatly from future studies measuring the force constants of amphibole and clinopyroxene with a range of $Fe^{3+}/\Sigma Fe$ ratios.

Our findings do not contradict previous studies that have suggested that prior isotopic depletion of the subarc mantle (Williams and Bizimis, 2014), oxygen fugacity (Williams et al., 2005; Dauphas et al., 2009), melt-peridotite reactions (Weyer and Ionov; 2007; Teng et al., 2011; Foden et al., 2018; Turner et al., 2018) and mantle metasomatism (Chen et al., 2023; Debret et al., 2016, 2018, 2020) exert strong controls over the Fe isotope systematics of arc magmas. Indeed, the Fe isotope composition of primary arc melts will be a function of the initial composition of the subarc mantle, temperature, and oxygen fugacity (Dauphas et al., 2009). Instead, we argue that the diversity in Fe isotope compositions observed in arc lavas also reflects important contributions from lower to mid-crustal fractionation, which act in concert with the variations in source composition discussed by many previous authors. The light Fe isotope ratios observed in many arc melts may also reflect fractionation of isotopically heavy magnetite and amphibole. At high melt fraction, mass balance dictates that the effects of fractionation on the Fe isotope composition of the crystallizing melt may be small if the majority of the system's Fe remains in the liquid. Cumulates may, therefore, also amplify trends towards lighter or heavier Fe isotope ratios that may not be resolvable in the lava record. Robust characterization of the Fe isotope dynamics in arcs requires integrating data from mantle residues, lavas, and cumulates for individual systems.

6. Conclusions

Fully characterizing the isotopic evolution of arc magmatic systems requires constraining $\delta^{56}Fe$ for the subarc mantle, erupted lavas, and crustal cumulates. We have shown that lower to mid-crustal cumulate xenoliths provide robust records of the Fe isotope systematics in evolving magmas. Our results highlight the important role differentiation may play in the isotopic evolution of arc systems. Fractionation of dunite and wehrlite cumulates may increase $\delta^{56}Fe$ of a differentiating melt, but once magnetite and amphibole saturation occur, removal of these isotopically heavy phases will decrease $\delta^{56}Fe$ in the melt. Only the latter interval of isotopic evolution (when melt MgO is < 6 wt%) is captured by the Adagdak lava record, emphasizing the importance of studying the complementary cumulate record. The light Fe isotope composition of a unique mantle dunite xenolith indicates that the subarc mantle beneath Adak experienced some depletion in heavy Fe isotopes, likely due to incompatible Fe^{3+} behavior during repeated episodes of partial melting, or reactions between mantle peridotite and mantle/slab-derived melts or fluids. Partial melting of this isotopically light mantle would have produced magmas with light $\delta^{56}Fe$ compositions, possible parental melts to the Adagdak dunite and wehrlite cumulates. Our

results highlight the importance of amphibole fractionation in influencing the Fe isotope evolution of hydrous arc systems. As an isotopically heavy phase ($\delta^{56}Fe$ = +0.07 to +0.09 ‰ in Adagdak cumulates) and major Fe reservoir in mid to upper-crustal cumulate assemblages (26–99 % of the bulk FeO_T budget for Adagdak amphibole gabbro and hornblendite cumulates), amphibole fractionation may play an important role in explaining the depleted nature of some erupted arc lavas relative to MORB.

Data availability

Data are available through Mendeley Data at: https://doi.org/10.17632/t2jct3f48y.1.

Declaration of competing interest

The authors declare that they have no known competing financial interests or personal relationships that could have appeared to influence the work reported in this paper.

Appendix A. Supplementary material

Two supplementary files are associated with this article. Supplementary tables containing major element (and when available, trace element) data corresponding to the Fe isotope analyses, Fe isotope composition of all measured USGS standards, and additional modeling information are given in an Excel document. Additional figures, an expanded discussion of SMS data collection and processing, and an expanded discussion of the Fe isotope modeling are given in a PDF

document. Supplementary material to this article can be found online at https://doi.org/10.1016/j.gca.2024.05.026.

References

Bai, Y., Su, B.X., Xiao, Y., Cui, M.M., Charlier, B., 2021. Magnesium and iron isotopic evidence of inter-mineral diffusion in ultramafic cumulates of the Peridotite Zone, Stillwater Complex. Geochim. Cosmochim. Acta 292, 152–169.

Barber, N.D., Edmonds, M., Jenner, F., Audétat, A., Williams, H., 2021. Amphibole control on copper systematics in arcs: Insights from the analysis of global datasets. Geochim. Cosmochim. Acta 307, 192–211.

Beard, B.L., Johnson, C.M., 2004. Inter-mineral Fe isotope variations in mantle-derived rocks and implications for the Fe geochemical cycle. Geochim. Cosmochim. Acta 68 (22), 4727–4743.

Blatter, D.L., Sisson, T.W., Hankins, W.B., 2013. Crystallization of oxidized, moderately hydrous arc basalt at mid-to lower-crustal pressures: implications for andesite genesis. Contrib. Mineral. Petrol. 166, 861–886.

Bryndzia, L.T., Wood, B.J., 1990. Oxygen thermobarometry of abyssal spinel peridotites; the redox state and C-O-H volatile composition of the Earth's sub-oceanic upper mantle. Am. J. Sci. Am. J. Sci. 290, 1093–1116.

Bucholz, C.E., Spencer, C.J., 2019. Strongly peraluminous granites across the Archean-Proterozoic transition. J. Petrol. 60 (7), 1299–1348.

Calvert, A.J., Klemperer, S.L., Takahashi, N., Kerr, B.C., 2008. Three-dimensional crustal structure of the Mariana Island arc from seismic tomography. J. Geophys. Res. Solid Earth 113 (B1).

Chen, Z., Chen, J., Tamehe, L.S., Zhang, Y., Zeng, Z., Zhang, T., Yin, X., 2023. Light Fe isotopes in arc magmas from cold subduction zones: Implications for serpentinite-derived fluids oxidized the sub-arc mantle. Geochim. Cosmochim. Acta 342, 1–14.

Chen, Y., Niu, Y., Xue, Q., Gao, Y., Castillo, P., 2021. An iron isotope perspective on back-arc basin development: Messages from Mariana Trough basalts. Earth Planet. Sci. Lett. 572, 117133.

Chen, L.M., Song, X.Y., Zhu, X.K., Zhang, X.Q., Yu, S.Y., Yi, J.N., 2014. Iron isotope fractionation during crystallization and sub-solidus re-equilibration: Constraints from the Baima mafic layered intrusion, SW China. Chem. Geol. 380, 97–109.

Citron, G.P., Kay, R.W., Kay, S.M., Snee, L.W., Sutter, J.F., 1980. Tectonic significance of early Oligocene plutonism on Adak Island, central Aleutian Islands, Alaska. Geology 8, 375–379.

Coats, R.R., 1952. Magmatic differentiation in Tertiary and Quaternary volcanic rocks from Adak and Kanaga islands, Aleutian Islands. Alaska. Geol. Soc. Am. Bull. 63 (5), 485–514.

Cooper, G.F., Blundy, J.D., Macpherson, C.G., Humphreys, M.C., Davidson, J.P., 2019. Evidence from plutonic xenoliths for magma differentiation, mixing and storage in a volatile-rich crystal mush beneath St. Eustatius, Lesser Antilles. Contrib. Mineral. Petrol. 174, 1–24.

Cooper, G.F., Inglis, E.C., 2022. A crustal control on the Fe isotope systematics of volcanic arcs revealed in plutonic xenoliths from the Lesser Antilles. Front. Earth Sci. 9, 795858.

Cooper, G.F., Davidson, J.P., Blundy, J.D., 2016. Plutonic xenoliths from Martinique, Lesser Antilles: evidence for open system processes and reactive melt flow in island arc crust. Contrib. Mineral. Petrol. 171, 1–21.

Cottrell, E., Birner, S.K., Brounce, M., Davis, F.A., Waters, L.E., Kelley, K.A., 2021. Oxygen fugacity across tectonic settings. Magma Redox Geochemistry 33–61.

Craddock, P.R., Dauphas, N., 2011. Iron isotopic compositions of geological reference materials and chondrites. Geostand. Geoanal. Res 35 (1), 101–123.

Dauphas, N., Janney, P.E., Mendybaev, R.A., Wadhwa, M., Richter, F.M., Davis, A.M., et al., 2004. Chromatographic separation and multicollection-ICPMS analysis of iron. Investigating mass-dependent and mass-independent isotope effects. Anal. Chem. 76 (19), 5855–5863.

Dauphas, N., Craddock, P.R., Asimow, P.D., Bennett, V.C., Nutman, A.P., Ohnenstetter, D., 2009. Iron isotopes may reveal the redox conditions of mantle melting from Archean to Present. Earth Planet. Sci. Lett. 288 (1–2), 255–267.

Dauphas, N., Roskosz, M., Alp, E.E., Golden, D.C., Sio, C.K., Tissot, F.L.H., et al., 2012. A general moment NRIXS approach to the determination of equilibrium Fe isotopic fractionation factors: application to goethite and jarosite. Geochim. Cosmochim. Acta 94, 254–275.

Dauphas, N., Roskosz, M., Alp, E.E., Neuville, D.R., Hu, M.Y., Sio, C.K., et al., 2014. Magma redox and structural controls on iron isotope variations in Earth's mantle and crust. Earth Planet. Sci. Lett. 398, 127–140.

Davis, F.A., Cottrell, E., Birner, S.K., Warren, J.M., Lopez, O.G., 2017. Revisiting the electron microprobe method of spinel-olivine-orthopyroxene oxybarometry applied to spinel peridotitesk. Am. Mineral. 102, 421–435.

Davis, A.S., Pickthorn, L.B.G., Valuer, T.L., Marlow, M.S., 1989. Petrology and age of volcanic-arc rocks from the continental margin of the Bering Sea: implications for Early Eocene relocation of plate boundaries. Can. J. Earth Sci. 26 (7), 1474–1490.

Debari, S., Kay, S.M., Kay, R.W., 1987. Ultramafic xenoliths from Adagdak volcano, Adak, Aleutian Islands, Alaska: deformed igneous cumulates from the Moho of an island arc. J. Geol 95 (3), 329–341.

Debret, B., Millet, M.A., Pons, M.L., Bouilhol, P., Inglis, E., Williams, H., 2016. Isotopic evidence for iron mobility during subduction. Geology 44 (3), 215–218.

Debret, B., Bouilhol, P., Pons, M.L., Williams, H., 2018. Carbonate transfer during the onset of slab devolatilization: New insights from Fe and Zn stable isotopes. J. Petrol. 59 (6), 1145–1166.

Debret, B., Reekie, C.D.J., Mattielli, N., Beunon, H., Ménez, B., Savov, I.P., Williams, H. M., 2020. Redox transfer at subduction zones: insights from Fe isotopes in the Mariana forearc. Geochem. Perspect. Lett. 46–51.

Demény, A., Vennemann, T.W., Harangi, S., Homonnay, Z., Fórizs, I., 2006. H2O-δD-FeIII relations of dehydrogenation and dehydration processes in magmatic amphiboles. Rapid Commun. Mass Spectrom. 20 (5), 919–925.

Deng, J., He, Y., Zartman, R.E., Yang, X., Sun, W., 2022. Large iron isotope fractionation during mantle wedge serpentinization: Implications for iron isotopes of arc magmas. Earth Planet. Sci. Lett. 583, 117423.

Du, D.H., Tang, M., Li, W., Kay, S.M., Wang, X.L., 2022. What drives Fe depletion in calc-alkaline magma differentiation: insights from Fe isotopes. Geology 50 (5), 552–556.

Dyar, M.D., McGuire, A.V., Harrell, M.D., 1992. Crystal chemistry of iron in two styles of metasomatism in the upper mantle. Geochim. Cosmochim. Acta 56 (6), 2579–2586.

Fabriès, J., 1979. Spinel-olivine geothermometry in peridotites from ultramafic complexes. Contrib. Mineral. Petrol. 69 (4), 329–336.

Foden, J., Sossi, P.A., Nebel, O., 2018. Controls on the iron isotopic composition of global arc magmas. Earth Planet. Sci. Lett. 494, 190–201.

Gaetani, G.A., Grove, T.L., 1998. The influence of water on melting of mantle peridotite. Contrib. Mineral. Petrol. 131, 323–346.

Green, D.H., Hibberson, W.O., Rosenthal, A., Kovács, I., Yaxley, G.M., Falloon, T.J., Brink, F., 2014. Experimental study of the influence of water on melting and phase assemblages in the upper mantle. J. Petrol 55 (10), 2067–2096.

Hao, X.L., Li, Y.L., 2013. 57Fe Mössbauer spectroscopy of mineral assemblages in mantle spinel lherzolites from Cenozoic alkali basalt, eastern China: Petrological applications. Lithos 156, 112–119.

Hawkesworth, C.J., Gallagher, K., Hergt, J.M., McDermott, F., 1993. Mantle and slab contributions in arc magmas. Annu. Rev. Earth Planet. Sci. 21 (1), 175–204.

Hawthorne, F.C., Oberti, R., Harlow, G.E., Maresch, W.V., Martin, R.F., Schumacher, J. C., Welch, M.D., 2012. Nomenclature of the amphibole supergroup. Am. Mineral. 97 (11–12), 2031–2048.

He, Y., Wu, H., Ke, S., Liu, S.A., Wang, Q., 2017. Iron isotopic compositions of adakitic and non-adakitic granitic magmas: Magma compositional control and subtle residual garnet effect. Geochim. Cosmochim. Acta 203, 89–102.

Holloway, J.R., Burnham, C.W., 1972. Melting relations of basalt with equilibrium water pressure less than total pressure. J. Petrol 13 (1), 1–29.

Jackson, J.M., Hamecher, E.A., Sturhahn, W., 2009. Nuclear resonant X-ray spectroscopy of (Mg, Fe) SiO3 orthoenstatites. Eur. J. Mineral. 21 (3), 551–560.

Janiszewski, H.A., Abers, G.A., Shillington, D.J., Calkins, J.A., 2013. Crustal structure along the Aleutian island arc: New insights from receiver functions constrained by active-source data. Geochem. Geophys. Geosyst. 14 (8), 2977–2992.

Jicha, B.R., Kay, S.M., 2018. Quantifying arc migration and the role of forearc subduction erosion in the central Aleutians. J. Volcanol. Geotherm. Res. 360, 84–99.

Jicha, B.R., Scholl, D.W., Singer, B.S., Yogodzinski, G.M., Kay, S.M., 2006. Revised age of Aleutian Island Arc formation implies high rate of magma production. Geology 34 (8), 661–664.

Johnson, A.C., Zhang, Z.J., Dauphas, N., Rudnick, R.L., Foden, J.D., Toc, M., 2023. Redox and mineral controls on Fe and Ti isotopic fractionations during calc-alkaline magmatic differentiation. Geochim. Cosmochim. Acta 355, 1–12.

Kay, S.M. and R.W. Kay, 1994, Aleutian magmatism in space and time, in G. Plafker and H.C. Berg (eds.), The Geology of Alaska, Decade of North American Geology (DNAG), Geological Society of America, v. G-1, p. 687-722.

Kay, S.M., Kay, R.W., Citron, G.P., 1982. Tectonic controls on tholeiitic and calc-alkaline magmatism in the Aleutian Arc. J. Geophys. Res. Solid Earth 87 (B5), 4051–4072.

Kay, S.M., Kay, R.W., 1985. Aleutian tholeiitic and calc-alkaline magma series I: the mafic phenocrysts. Contrib. Mineral. Petrol. 90, 276–290.

Kay, S., Kay, R., Citron, G.P., Perfit, M.R., 1990. Calc-alkaline plutonism in the intra-oceanic Aleutian arc, Alaska. Plutonism from Antarctica to Alaska. Geol. Soc. Am. Special Paper 241, 233–256.

Kay, S.M., Mpodozis, C., 2001. Central Andean ore deposits linked to evolving shallow subduction systems and thickening crust. GSA Today 11 (3), 4.

Kay, S.M., Mpodozis, C., Ramos, V.A., Munizaga, F., 1991. Magma source variations for mid-late Tertiary magmatic rocks associated with a shallowing subduction zone and a thickening crust in the central Andes (28 to 33 S). Geol. Soc. Am. Spec. Pap. 265, 113–137.

Kay, S.M., Jicha, B.R., Citron, G.L., Kay, R.W., Tibbetts, A.K., Rivera, T.A., 2019. The Calc-Alkaline Hidden Bay and Kagalaska Plutons and the Construction of the Central Aleutian Oceanic Arc Crust. J. Petrol. 60, 393–439.

Krawczynski, M.J., Grove, T.L., Behrens, H., 2012. Amphibole stability in primitive arc magmas: effects of temperature, H2O content, and oxygen fugacity. Contrib. Mineral. Petrol. 164 (2), 317–339.

Kress, V.C., Carmichael, I.S., 1991. The compressibility of silicate liquids containing Fe 2 O 3 and the effect of composition, temperature, oxygen fugacity and pressure on their redox states. Contrib. Mineral. Petrol. 108, 82–92.

Lehmann, J., 1983. Diffusion between olivine and spinel: application to geothermometry. Earth Planet. Sci. Lett. 64 (1), 123–138.

Lewis, M.J., Bucholz, C.E., Jagoutz, O.E., 2021. Evidence for polybaric fractional crystallization in a continental arc: Hidden Lakes mafic complex, Sierra Nevada batholith, California. Contrib. Mineral. Petrol. 176, 1–27.

Li, Q.W., Zhao, J.H., Wang, Q., Zhang, Z.F., An, Y.J., He, Y.T., 2020. Iron isotope fractionation in hydrous basaltic magmas in deep crustal hot zones. Geochim. Cosmochim. Acta 279, 29–44.

Liermann, H.P., Ganguly, J., 2002. Diffusion kinetics of Fe2+ and Mg in aluminous spinel: experimental determination and applications. Geochim. Cosmochim. Acta 66 (16), 2903–2913.

Luth, R.W., Canil, D., 1993. Ferric iron in mantle-derived pyroxenes and a new oxybarometer for the mantle. Contrib. Mineral. Petrol. 113 (2), 236–248.

Makino, K., Tomita, K., 1989. Cation distribution in the octahedral sites of hornblendes. Am. Mineral. 74, 1097–1105.

Mandler, B.E., Grove, T.L., 2016. Controls on the stability and composition of amphibole in the Earth's mantle. Contrib. Mineral. Petrol. 171, 1–20.

Marxer, F., Ulmer, P., Müntener, O., 2022. Polybaric fractional crystallisation of arc magmas: an experimental study simulating trans-crustal magmatic systems. Contrib. Mineral. Petrol. 177 (1), 3.

Müntener, O., Kelemen, P.B., Grove, T.L., 2001. The role of H 2 O during crystallization of primitive arc magmas under uppermost mantle conditions and genesis of igneous pyroxenites: an experimental study. Contrib. Mineral. Petrol. 141, 643–658.

Müntener, O., Ulmer, P., 2018. Arc crust formation and differentiation constrained by experimental petrology. Am. J. Sci. 318 (1), 64–89.

Myers, J.D., Marsh, B.D., Sinha, A.K., 1985. Strontium isotopic and selected trace element variations between two Aleutian volcanic centers (Adak and Atka): implications for the development of arc volcanic plumbing systems. Contrib. Mineral. Petrol. 91, 221–234.

Nandedkar, R.H., Ulmer, P., Müntener, O., 2014. Fractional crystallization of primitive, hydrous arc magmas: an experimental study at 0.7 GPa. Contrib. Mineral. Petrol. 167, 1015.

Nebel, O., Arculus, R.J., Sossi, P.A., Jenner, F.E., Whan, T.H., 2013. Iron isotopic evidence for convective resurfacing of recycled arc-front mantle beneath back-arc basins. Geophys. Res. Lett. 40 (22), 5849–5853.

Nebel, O., Sossi, P.A., Bénard, A., Wille, M., Vroon, P.Z., Arculus, R.J., 2015. Redox-variability and controls in subduction zones from an iron-isotope perspective. Earth Planet. Sci. Lett. 432, 142–151.

Nie, N.X., Dauphas, N., Alp, E.E., Zeng, H., Sio, C.K., Hu, J.Y., et al., 2021. Iron, magnesium, and titanium isotopic fractionations between garnet, ilmenite, fayalite, biotite, and tourmaline: Results from NRIXS, ab initio, and study of mineral separates from the Moosilauke metapelite. Geochim. Cosmochim. Acta 302, 18–45.

Nielsen, S.G., Yogodzinski, G., Prytulak, J., Plank, T., Kay, S.M., Kay, R.W., Kading, T., 2016. Tracking along-arc sediment inputs to the Aleutian arc using thallium isotopes. Geochim. Cosmochim. Acta 181, 217–237.

Ozawa, K., 1984. Olivine-spinel geospeedometry: Analysis of diffusion-controlled Mg-Fe2+ exchange. Geochim. Cosmochim. Acta 48 (12), 2597–2611.

Pichavant, M., Macdonald, R., 2007. Crystallization of primitive basaltic magmas at crustal pressures and genesis of the calc-alkaline igneous suite: experimental evidence from St Vincent, Lesser Antilles arc. Contrib. Mineral. Petrol. 154, 535–558.

Poitrasson, F., Delpech, G., Grégoire, M., 2013. On the iron isotope heterogeneity of lithospheric mantle xenoliths: implications for mantle metasomatism, the origin of basalts and the iron isotope composition of the Earth. Contrib. Mineral. Petrol. 165, 1243–1258.

Polyakov, V.B., Mineev, S.D., 2000. The use of Mössbauer spectroscopy in stable isotope geochemistry. Geochim. Cosmochim. Acta 64 (5), 849–865.

Polyakov, V.B., Clayton, R.N., Horita, J., Mineev, S.D., 2007. Equilibrium iron isotope fractionation factors of minerals: reevaluation from the data of nuclear inelastic resonant X-ray scattering and Mössbauer spectroscopy. Geochim. Cosmochim. Acta 71 (15), 3833–3846.

Prissel, K., Olive, J.A., Krawczynski, M.J., 2023. A Log-Ratio-Based Algorithm for Petrologic Mass-Balance Problems and Uncertainty Assessment. Geochem. Geophys. Geosyst. 24 (12).

Ratschbacher, B.C., Jackson, J.M., Toellner, T.S., Bucholz, C.E., Sturhahn, W., Solomatova, N.V., 2023. Fe³⁺/Feᵀ ratios of amphiboles determined by high spatial resolution single-crystal synchrotron Mössbauer spectroscopy. Am. Mineral. 108 (1), 70–86.

Romick, J.D., Kay, S.M., Kay, R.W., 1992. The influence of amphibole fractionation on the evolution of calc-alkaline andesite and dacite tephra from the central Aleutians. Alaska. Contrib. Mineral. Petrol. 112, 101–118.

Roskosz, M., Sio, C.K., Dauphas, N., Bi, W., Tissot, F.L., Hu, M.Y., et al., 2015. Spinel-olivine-pyroxene equilibrium iron isotopic fractionation and applications to natural peridotites. Geochim. Cosmochim. Acta 169, 184–199.

Roskosz, M., Dauphas, N., Hu, J., Hu, M.Y., Neuville, D.R., Brown, D., et al., 2022. Structural, redox and isotopic behaviors of iron in geological silicate glasses: A NRIXS study of Lamb-Mössbauer factors and force constants. Geochim. Cosmochim. Acta 321, 184–205.

Rouxel, O., Dobbek, N., Ludden, J., Fouquet, Y., 2003. Iron isotope fractionation during oceanic crust alteration. Chem. Geol. 202 (1–2), 155–182.

Rouxel, O., Shanks III, W.C., Bach, W., Edwards, K.J., 2008. Integrated Fe-and S-isotope study of seafloor hydrothermal vents at East Pacific Rise 9–10 N. Chem. Geol. 252 (3–4), 214–227.

Schoenberg, R., Marks, M.A., Schuessler, J.A., von Blanckenburg, F., Markl, G., 2009. Fe isotope systematics of coexisting amphibole and pyroxene in the alkaline igneous rock suite of the Ilímaussaq Complex. South Greenland. Chem. Geol. 258 (1–2), 65–77.

Scholl, D.W., Buffington, E.C., Marlow, M.S., 1975. Plate tectonics and the structural evolution of the Aleutian-Bering Sea region, in Forbes, R. B., ed., Contributions to the geology of the Bering Sea Basin and adjacent regions. Geol. Soc. Am. Spec. Pap. 151, 1–31.

Sisson, T.W., Grove, T.L., 1993. Experimental investigations of the role of H 2 O in calc-alkaline differentiation and subduction zone magmatism. Contrib. Mineral. Petrol. 113, 143–166.

Sosa, E.S., Bucholz, C.E., Barickman, M.H., VanTongeren, J.A., Setera, J.B., Kay, S.M., Kay, R.W., 2023. Petrology and geochemistry of Adak Island plutonic xenoliths: implications for primitive magma generation and crustal differentiation in the Aleutian Island arc. J. Petrol. 64 (10).

Sossi, P.A., Foden, J.D., Halverson, G.P., 2012. Redox-controlled iron isotope fractionation during magmatic differentiation: an example from the Red Hill intrusion. S. Tasmania. Contrib. Mineral. Petrol. 164 (5), 757–772.

Sossi, P.A., O'Neill, H.S.C., 2017. The effect of bonding environment on iron isotope fractionation between minerals at high temperature. Geochim. Cosmochim. Acta 196, 121–143.

Stamper, C.C., Melekhova, E., Blundy, J.D., Arculus, R.J., Humphreys, M.C.S., Brooker, R.A., 2014. Oxidised phase relations of a primitive basalt from Grenada, Lesser Antilles. Contrib. Mineral. Petrol. 167, 1–20.

Sturhahn, W., 2000. CONUSS and PHOENIX: Evaluation of nuclear resonant scattering data. Hyperfine Interact. 125, 149–172.

Sturhahn, W. (2021): CONUSS (Coherent Nuclear Scattering by Single crystals). Open-source software. http://www.nrixs.com.

Teng, F.Z., Dauphas, N., Helz, R.T., Gao, S., Huang, S., 2011. Diffusion-driven magnesium and iron isotope fractionation in Hawaiian olivine. Earth Planet. Sci. Lett. 308 (3–4), 317–324.

Teng, F.Z., Dauphas, N., Huang, S., Marty, B., 2013. Iron isotopic systematics of oceanic basalts. Geochim. Cosmochim. Acta 107, 12–26.

Turner, S., Williams, H., Piazolo, S., Blichert-Toft, J., Gerdes, M., Adam, J., Maury, R., 2018. Sub-arc xenolith Fe-Li-Pb isotopes and textures tell tales of their journey through the mantle wedge and crust. Geology 46 (11), 947–950.

Ulmer, P., Kaegi, R., Müntener, O., 2018. Experimentally Derived Intermediate to Silica-rich Arc Magmas by fractional and equilibrium crystallization at 1·0 GPa: an evaluation of phase relationships, compositions, liquid lines of descent and oxygen fugacity. J. Petrol. 59, 11–58.

Vogt, K., Dohmen, R., Chakraborty, S., 2015. Fe-Mg diffusion in spinel: New experimental data and a point defect model. Am. Mineral. 100 (10), 2112–2122.

Wasylenki, L.E., Baker, M.B., Kent, A.J., Stolper, E.M., 2003. Near-solidus melting of the shallow upper mantle: partial melting experiments on depleted peridotite. J. Petrol 44 (7), 1163–1191.

Weyer, S., Ionov, D.A., 2007. Partial melting and melt percolation in the mantle: the message from Fe isotopes. Earth Planet. Sci. Lett. 259 (1–2), 119–133.

Williams, H.M., Bizimis, M., 2014. Iron isotope tracing of mantle heterogeneity within the source regions of oceanic basalts. Earth Planet. Sci. Lett. 404, 396–407.

Williams, H.M., McCammon, C.A., Peslier, A.H., Halliday, A.N., Teutsch, N., Levasseur, S., Burg, J.P., 2004. Iron isotope fractionation and the oxygen fugacity of the mantle. Science 304 (5677), 1656–1659.

Williams, H.M., Peslier, A.H., McCammon, C., Halliday, A.N., Levasseur, S., Teutsch, N., Burg, J.P., 2005. Systematic iron isotope variations in mantle rocks and minerals: the effects of partial melting and oxygen fugacity. Earth Planet. Sci. Lett. 235 (1–2), 435–452.

Williams, H.M., Prytulak, J., Woodhead, J.D., Kelley, K.A., Brounce, M., Plank, T., 2018. Interplay of crystal fractionation, sulfide saturation and oxygen fugacity on the iron isotope composition of arc lavas: An example from the Marianas. Geochim. Cosmochim. Acta 226, 224–243.

Wood, B.J., Virgo, D., 1989. Upper mantle oxidation state: Ferric iron contents of lherzolite spinels by 57Fe Mössbauer spectroscopy and resultant oxygen fugacities. Geochim. Cosmochim. Acta 53 (6), 1277–1291.

Woodland, A.B., 2009. Ferric iron contents of clinopyroxene from cratonic mantle and partitioning behaviour with garnet. Lithos 112, 1143–1149.

Yogodzinski, G.M., Kelemen, P.B., 2007. Trace elements in clinopyroxenes from Aleutian xenoliths: Implications for primitive subduction magmatism in an island arc. Earth Planet. Sci. Lett. 256 (3–4), 617–632.

Zhao, X., Zhang, H., Zhu, X., Tang, S., Tang, Y., 2010. Iron isotope variations in spinel peridotite xenoliths from North China Craton: implications for mantle metasomatism. Contrib. Mineral. Petrol. 160, 1–14.

Zhao, X., Zhang, H., Zhu, X., Tang, S., Yan, B., 2012. Iron isotope evidence for multistage melt-peridotite interactions in the lithospheric mantle of eastern China. Chem. Geol. 292, 127–139.

Zhao, X.M., Zhang, H.F., Zhu, X.K., Zhu, B., Cao, H.H., 2015. Effects of melt percolation on iron isotopic variation in peridotites from Yangyuan, North China Craton. Chem. Geol. 401, 96–110.